

NUMERICAL STUDY OF THERMAL-HYDRAULIC-MECHANICAL
BEHAVIOR OF FRACTURED GEOTHERMAL RESERVOIRS

by

Shihao Wang

Copyright by Shihao Wang, 2014

All Rights Reserved

A thesis submitted to the Faculty and the Board of Trustees of the Colorado School of Mines in partial fulfillment of the requirements for the degree of Master of Science (Petroleum Engineering).

Golden, Colorado

Date _____

Signed: _____
Shihao Wang

Signed: _____
Dr. Yu-Shu Wu
Thesis Advisor

Golden, Colorado

Date: _____

Signed: _____
Dr. Erdal Ozkan
Professor and Head
Department of Petroleum Engineering

ABSTRACT

This work aims to develop powerful numerical tools to study the thermal-hydraulic-mechanical (THM) behavior of fractured geothermal reservoirs. It contains three parts: a massively parallel fully coupled THM simulator, a semi-analytical correlation to capture the thermal induced fracture aperture change and the multistage preconditioning used for THM simulation.

A massively-parallel, fully-coupled THM simulator, THM-EGS, has been developed and verified. The simulator is written in Fortran 03 and the governing equations are solved using Integral Finite Difference Method (IFD). Mechanical deformation effects are captured by solving a mean stress equation, derived from the equations governing deformation of porous media. This equation is computationally efficient and accurate enough for reservoir flow applications. The simulator has an efficient parallel computation scheme using MPI for communication between processes.

A novel correlation of the thermal-induced normal change of fracture aperture has been derived. The new correlation is based on the solution of the governing displacement equations. Compared to the existing empirical correlations, the new correlation can better describe the physical processes. The new correlation can also be applied to elastic-plastic fractures. We have implemented this correlation in THM-EGS. The correlation has been used to study the permeability enhancement effect of a hydraulically connected well pair. The results are that the permeability will be enhanced by as large as 2 orders of magnitude. The results of this study have the potential to guide the operations of geothermal reservoirs.

We will also investigate multi-stage preconditioning in THM simulation. We will implement a Constraint Pressure Residual (CPR) type multistage preconditioner into the linear solver of THM-EGS. In the multistage preconditioner, the fluid, energy and mechanical equation are preconditioned with different strategies based on their own unique feature. The multistage preconditioner has been tested on both homogeneous and heterogeneous problems. It has greatly improved the numerical performance of the linear solver, especially for highly heterogeneous problems.

TABLE OF CONTENTS

ABSTRACT.....	III
LIST OF FIGURES	VIII
LIST OF TABLES.....	XI
LIST OF SYMBOLS	XII
LIST OF ABBRIEVATIONS.....	XIV
ACKNOWLEDGEMENTS.....	XV
CHAPTER 1 INTRODUCTION.....	1
1.1 General Aspects Of The Problem	1
1.2 Thesis Objectives.....	1
1.3 Thesis Layout.....	2
CHAPTER 2 BACKGROUND.....	4
2.1 General Background of Geothermal Engineering.....	4
2.2 Fracture Characterization	6
2.3 Mechanical Behavior of Fractures	8
2.4 Multi-physics Coupling Strategies.....	10
2.5 Linear Solver and Multistage Preconditioning	12
CHAPTER 3 METHODOLOGY	14
3.1 Formulation of Fluid and Heat Flow.....	14
3.2 Formulation of Geomechanics Module.....	15
3.3 Fluid Properties	18
3.4 Mechanical Properties.....	18
3.5 Numerical Approach	20

CHAPTER 4	SEMI-ANALYTICAL ANALYSIS OF FRACTURE APERTURE	22
4.1	Limitations of Existing Fracture Aperture Models	22
4.2	Derivation of the Correlation	23
4.3	Sensitivity Analysis And Elastic-Plastic Extension	28
CHAPTER 5	SIMULATOR DEVELOPMENT AND VERIFICATION	33
5.1	Fully Coupled Multi-Physics Coupling Framework	33
5.2	Equation-of-state (EOS) module and primary variables	34
5.3	Parallel framework	35
5.3.1	Parallel Preprocessing	35
5.3.2	Parallel Simulation	37
5.3.3	Parallel Jacobian Construction and Optimized Memory Storage	41
5.4	Simulator Verification	41
5.4.1	2-Dimensional Compaction with Mandel-Cryer Effect	41
5.4.2	Field-Scale Case with Over a Million of Grid Blocks	44
CHAPTER 6	NUMERICAL STUDY OF COLD WATER INJECTION	49
6.1	Homogeneous Case with Higher Permeability	49
6.2	Homogeneous Case with Lower Permeability	54
6.3	Sensitivity Analysis of Injection Temperature and Injection Rate	56
6.4	Extremely Low Permeable HDR with Fractured Zone	60
CHAPTER 7	MULTISTAGE PRECONDITIONING FOR THM PROBLEMS	63
7.1	Frequency of THM Coupled Problem	63
7.2	Description of Algorithm	64
7.3	Homogeneous Case	66

7.4	Homogeneous Case with Fractured Zone	68
7.5	Highly Heterogeneous Case	70
CHAPTER 8	CONCLUSION AND DISCUSSION	73
8.1	Summary and Conclusion	73
8.2	Suggestions for future work	74
APPENDIX A	WATER PROPERTIES IN THM-EGS	83
APPENDIX B	GAS PROPERTY IN THM-EGS.....	85
APPENDIX C	AN EXAMPLE INPUT FILE FOR THM-EGS.....	87

LIST OF FIGURES

Figure 2-1	Geothermal resources at the depth of 10km in the United States.....	4
Figure 2-2	World's geothermal electricity generation growth.....	5
Figure 2-3	Conceptual model of Enhanced Geothermal System.....	5
Figure 2-4	Definition of fracture aperture	7
Figure 2-5	The aperture distribution of the fracture surface of Hwangdeung granite.....	7
Figure 2-6	Interaction among the THM processes.....	10
Figure 3-1	Integral finite difference method on REV.....	21
Figure 4-1	Scale effect of mechanical normal closure.....	22
Figure 4-2	Conceptual model of fracture surrounded matrix block.....	23
Figure 4-3	Coceptual model of fracture resistance.....	25
Figure 4-4	Relationship between mechanical aperture and hydraulic aperture.....	27
Figure 4-5	Comparison between matrix temperature and center temperature.....	30
Figure 4-6	Fracture aperture change versus time.....	30
Figure 4-7	Fracture aperture change with different thermal expansion coefficients.....	31
Figure 4-8	Resistance-deformation curve of plastic-elastic example.....	31
Figure 4-9	Fracture aperture with elastic-plastic resistance.....	32
Figure 5-1	Data structure of element-based data types.....	34
Figure 5-2	Flowchart of parallel preprocessing part of the simulator.....	39
Figure 5-3	Flow chart of the whole simulator.....	40
Figure 5-4	Problem description of 2-dimensional compaction.....	42
Figure 5-5	Partitioned graph of the 2-D compaction case.....	43
Figure 5-6	Comparison between numerical results and numerical results.....	44

Figure 5-7	Problem description of the large reservoir case.....	45
Figure 5-8	Parallel speedup of THM-EGS and ideal performance.....	46
Figure 6-1	Site location map of the interested field in Cooper Basin.....	50
Figure 6-2	Three hydraulic connected wells in Cooper Basin.....	50
Figure 6-3	Problem setup in the simulator.....	51
Figure 6-4	Permeability change after cold water injection of Case 1.....	53
Figure 6-5	Pressure and permeability curve at cold water injector of Case 1.....	54
Figure 6-6	Fracture aperture and fracture permeability of Case 1.....	54
Figure 6-7	Permeability change after cold water injection of Case 2.....	55
Figure 6-8	Fracture aperture and fracture permeability curve of Case 2.....	56
Figure 6-9	Fracture aperture with different injection temperature.....	57
Figure 6-10	Fracture permeability with different injection temperature.....	57
Figure 6-11	Matrix permeability with respect to different injection temperature.....	58
Figure 6-12	Sensitivity of fracture stiffness.....	58
Figure 6-13	Fracture aperture with different injection rate at Case 3.....	59
Figure 6-14	Fracture permeability with different injection rate of Case 3.....	59
Figure 6-15	Conceptual model of fast flow channel in high-permeability zone.....	61
Figure 6-16	Permeability change after cold water injection of Case 3.....	61
Figure 6-17	Fracture permeability inside the fractured zone.....	62
Figure 7-1	Comparison between temperature field and pressure field.....	64
Figure 7-2	Performance of the multi-stage preconditioning of Case 1.....	67
Figure 7-3	Comparison of the numerical performance of Case 1.....	67
Figure 7-4	Homogenous permeability field with fractured zone.....	68

Figure 7-5	Performance of the multi-stage preconditioning of Case 2.....	69
Figure 7-6	Comparison of the numerical performance of Case 2.....	69
Figure 7-7	Heterogeneous permeability field.....	71
Figure 7-8	Performance of the multi-stage preconditioning of Case 3.....	71
Figure 7-9	Comparison of the numerical performance of Case 3.....	72
Figure 8-1	Limitation of the proposed model.....	74

LIST OF TABLES

Table 4-1	Parameters for calculating matrix temperature and aperture change.....	29
Table 5-1	Input parameters for 2-D compaction case.....	42
Table 5-2	Summary of computation configuration and performance.....	46
Table 5-3	Summary of the number of inner and border elements.....	47
Table 6-1	Input parameters for high-permeability case.....	52

LIST OF SYMBOLS

A	area of a connection
b_i	fracture aperture on the i th direction
E	Young's modulus
F	flux term
G	shear modulus
g	gravity terms
h	enthalpy
K	absolute permeability
K_r	relative permeability
K_R	formation heat conductivity
K_β	liquid heat conductivity
L_i	fracture spacing on the i th direction
M	accumulation term
Q	generation term
p	pore pressure
P_c	capillary pressure
S	phase saturation
T	temperature
T_f	fracture temperature
T_m	matrix temperature
T_{ref}	reference temperature

Δt	length of time step
\vec{u}	displacement vector
u	phase specific internal energy
V	volume
X	mass component
α	Biot's coefficient
β	thermal expansion coefficient
ε_k	diagonal strain component
ε_v	volumetric strain
ε_{kk}	diagonal strain component
λ	Lame's coefficient
μ	viscosity
$v_{max,hor}$	maximum horizontal stress
$v_{min,hor}$	minimum horizontal stress
ρ	density
σ	effective stress
σ_k	normal stress at the k th direction
σ_{kk}	diagonal stress component
σ_m	mean stress
σ_n	normal effective stress
\emptyset	porosity

LIST OF ABBREVIATIONS

Constraint Pressure Residual.....	CPR
Discrete Fracture Network.....	DFN
Enhanced Geothermal System.....	EGS
Hot Dry Rock.....	HDR
Integral Finite Difference.....	IFD
Joint Roughness Coefficient.....	JRC
Multiple Interacting Continua.....	MINC
Message Passing Interface.....	MPI
Thermal-Hydraulic-Mechanical.....	THM

ACKNOWLEDGEMENTS

I would like to express the deepest gratitude to my advisor, Dr. Yushu Wu, for his kind support throughout this work. Special thanks are due to Dr. Philip Winterfeld for his suggestion and correction, and Dr. Luis Zerpa for his guidance during each discussion.

I am very thankful to Department of Energy, without whose financial support this work can never be fulfilled. Foundation CMG also supports my study and offers me the opportunity to present in their conference, where I got the chance to discuss about my ideas with many excellent researchers.

I also want to thank all my friends in Energy Modeling Group and the whole PE department, and also friends in my life. I am happy to be the friend of Tiande, Wanli and many more. We all had a great time with each other's companion.

My sincere appreciation is extended to Ms. Denise Winn-Bower and Ms. Emilia Clayton for their efforts in the management of this project.

Contributions of many fellow research workers in the related area of reservoir engineering and high performance computation are acknowledged through the references cited. Especially, I am very thankful to Dr. Timothy Kaiser for his help on hybrid MPI/OPENMP computing. His patient instruction led me into an entire new world of high performance computing.

CHAPTER 1

INTRODUCTION

1.1 General Aspects of the Problem

Energy recovery from geothermal reservoirs involves multiple physical processes, including multiphase fluid flow, heat transfer, and rock deformation. To accurately capture these highly nonlinear THM effects, the numerical simulation would require millions of grid blocks with each grid block containing several primary variables, resulting in a very large number of equations that is expensive to solve. Therefore, massively parallel simulator and strong linear solve are absolutely necessary for large scale geothermal reservoir simulations.

Fractured Enhanced Geothermal System (EGS) reservoirs are typically sensitive to thermal and mechanical change induced by cold water injection. It has been observed that the permeability at the cold water injector will be significantly enhanced. The physical process behind this phenomena is that, the cold water injectors lowers the temperature of the reservoir and causes the matrix block to shrink, resulting in an increase of the fracture aperture and fracture permeability. As such, it is of great importance to quantify the effect of thermally induced fracture aperture change.

1.2 Thesis Objectives

The purpose of this work is to improve the understanding of fractured reservoir, using advanced numerical tools. To achieve this goal, the objectives of this work are as follows.

- Review the existing fracture aperture correlations.
- Develop a novel fracture aperture correlation to predict the thermal induced fracture aperture change more accurately.

- Develop a fully coupled thermal-hydraulic-mechanical reservoir simulator
- Parallelize the simulator to utilize it to reservoir scale problems
- Improve the stability and speed of the linear solver in the simulator using multistage preconditioning techniques.
- Investigate the permeability enhancement effect induced by cold water injection.

1.3 Thesis Layout

This thesis is organized as follows.

In Chapter 2, we will provide general background of this work. We will introduce the basic features of geothermal reservoirs, specifying the similarity between geothermal reservoirs and oil reservoirs. We will also review the existing model of fracture characterization and the coupling strategies of THM problems.

In Chapter 3, we will introduce the mathematical and numerical approaches used in this work, including the governing equations of fluid/heat flow, the mean stress method for mechanical simulation and the Integral Finite Difference method.

In Chapter 4, we will derive the fracture aperture correlation using analytical approach. We will investigate the possibility of extending the correlation to elastic-plastic problems.

In Chapter 5, we will describe the entire design of our newly developed geothermal simulator, THM-EGS. We will introduce its data structure, parallel framework and EOS module. We will also provide two cases to show the simulator's accuracy and parallel performance respectively.

In Chapter 6, we will use the simulator and the proposed correlation to study the permeability enhancement effect induced by cold water injection into fractured reservoirs. We

will investigate the difference of behaviors between the fracture and the matrix rock. We will also quantify the effect of injection rate and injection temperature respectively.

In Chapter 7, we will propose a multistage preconditioner for THM coupled problem. We will adapt the Constraint Pressure Residual (CPR) type preconditioner and implement the new preconditioner into THM-EGS. We will test the preconditioner in homogeneous and heterogeneous problems and compare their numerical performance.

CHAPTER 2 BACKGROUND

2.1 General Background of Geothermal Engineering

As thermal energy stored underground, geothermal energy is clean and renewable. As shown in Figure 2-1, huge amounts of potential geothermal resource exists in the mid-west area of the United States at the depth of 10km. Geothermal engineering strives for mining such energy using reservoir engineering technologies to generate electricity or supply heat. Geothermal industry is fast developing and very promising. As demonstrated by Figure 2-2 on page 5, the capacity of electricity generation with geothermal energy has increased more than 400% within the past forty years.



Figure 2-1 Geothermal resources at the depth of 10km in the United States (Tester et al., 2006).

A special kind of geothermal engineering technologies is Enhanced Geothermal Systems (EGS). EGS are engineered geothermal reservoirs. Basically, in EGS reservoirs, fractures are created on matrix rocks with low permeability. In some EGS reservoirs, fractures are directly engineered on Hot Dry Rocks (HDR). Once fractures are engineered, people create hydraulically connected wells in the fractured network by injecting cold water in injection wells

(cold water injectors) and producing hot water from production wells (hot water injectors). A conceptual model of such a system is shown in Figure 2-3.

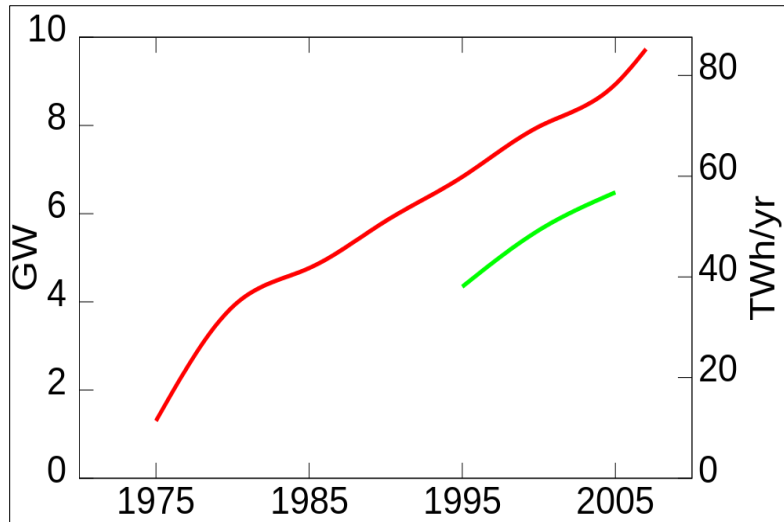


Figure 2-2 World's geothermal electricity generation growth (Bertani, 2007; Fridleifsson et al., 2008). Red line: installed capacity of electricity generation; green line: realized production.

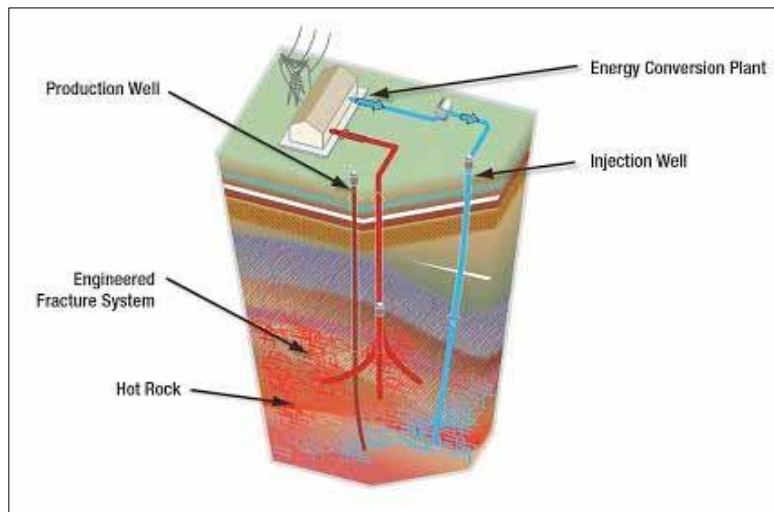


Figure 2-3 Conceptual model of Enhanced Geothermal System (Bertani, 2007, 2012).

The main flow path in EGS reservoirs is the engineered fractures, therefore the behaviors of fractures are crucial to the production of EGS reservoirs. In some enhanced geothermal

reservoirs with HDR, the matrix permeability is extremely low and the flow in fractures dominates the production rate.

Many features of EGS reservoirs, including their low matrix permeability and rock properties, are similar to those of certain types of oil/gas reservoirs, especially the unconventional reservoirs. Therefore, the research of geothermal reservoirs can also provide guide to petroleum reservoir engineering.

As mentioned above, fractures are important to geothermal reservoirs. Many types of fractures are sensitive to changing pressure and stresses, especially natural fractures that are penetrated by wells or re-activated by hydraulic fractures. Meanwhile, cold water injection can cause the matrix to shrink and the aperture of the surrounding fractures will be thus increased, resulting in an enhancement of permeability at the area that is close to the injector. The thermal-hydro-mechanical effects of injection and production can dramatically change the properties of fractures (Gelet et al., 2012), or even close some of them, resulting in a huge variation in the conductivity (Settari and Mourits, 1998; Settari and Walters, 2001; Jaeger and Zimmerman, 2009; Wu et al., 2011).

Considering the above reasons, the hydro-mechanical behaviors of the fractures are very important and should be thoroughly investigated.

2.2 Fracture Characterization

In reservoir engineering, fracture aperture is widely used to quantify the opening of fractures. However, as the walls of fracture are typically not smooth, the fracture aperture cannot be simply treated as the perpendicular width of fracture openings, as shown in the following Figure 2-4. The fracture aperture is subject to the fracture wall roughness and degree of mineral

infill and characterized by statistical approach using seismic or core scanning, as shown in Figure 2-5.

In industrial applications, the fracture aperture is treated as the average perpendicular width of fracture for a certain length.

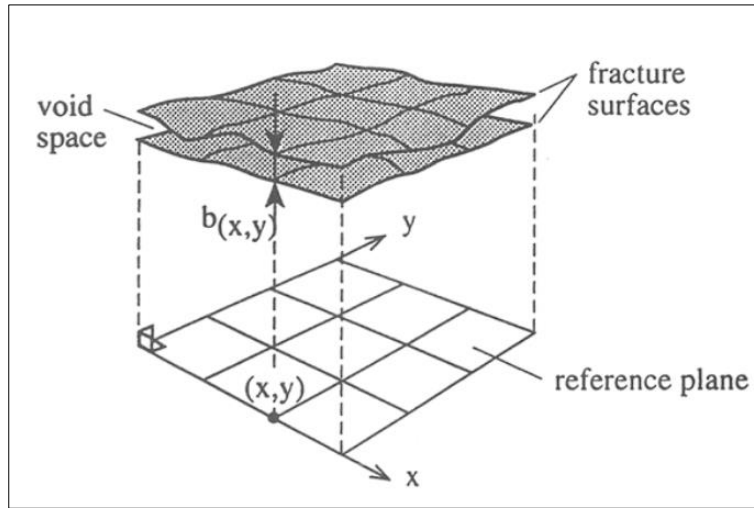


Figure 2-4 Definition of fracture aperture (Hakami and Larsson, 1996). Fracture aperture at point (x,y) is represented by $b(x,y)$.

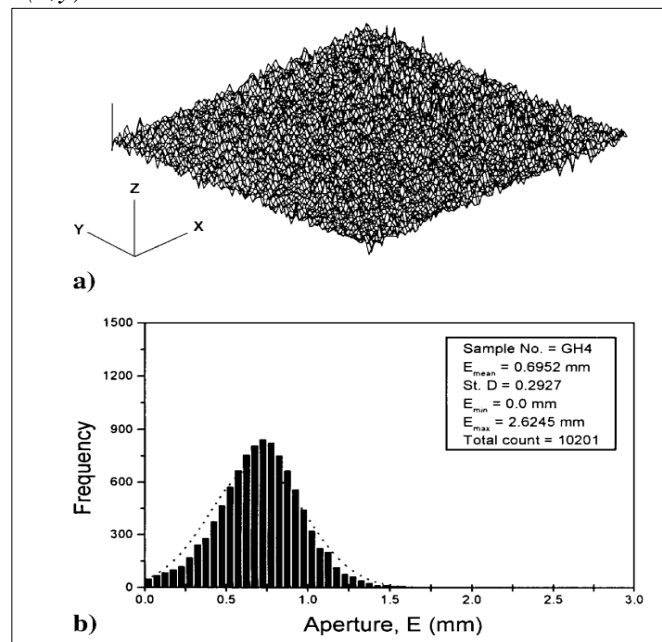


Figure 2-5. The aperture distribution of the fracture surface of Hwangdeung granite. Upper figure: the fracture aperture; lower figure: aperture frequency (Lee and Cho, 2002).

Besides fracture aperture, several parameters can be used to characterize the properties of fractures, in which the joint roughness coefficient (JRC) and the fracture stiffness are the most widely adopted parameters. The joint roughness coefficient is used to characterize the wall geometry of the fractures and can be obtained from direct shear stress tests. A large JRC indicates that the fracture is rough in its surface, so that the fracture is difficult to slide in the shear direction. The normal stiffness k_n and the shear stiffness k_t are first brought out by Goodman (1974). The normal and shear stiffness is defined in Equation (2.1) and (2.2) respectively

$$k_n = \frac{\partial \sigma_n}{\partial u_n} \quad (2.1)$$

$$k_t = \frac{\partial \sigma_t}{\partial u_t} \quad (2.2)$$

where σ is the stress and u is the displacement. n and t refers to normal and shear direction respectively.

2.3 Mechanical Behavior of Fractures

Several experiments (Goodman, 1974; Wilson and Aifanti, 1982) have been conducted to investigate the mechanical behavior of the normal closure of fractures. There are mainly two types of models, known as the hyperbolic model and the logarithmic model, to correlate the fracture aperture with the stress. The change of fracture aperture results in a variation of the permeability/transmissibility of fractures.

Among the correlations belonging to the hyperbolic model, the Barton-Bandis' correlation (Bandis et al., 1983; Barton et al., 1985; Bandis, 1990) is the most widely used one, as shown in the following equation.

$$\Delta b = \frac{\Delta \sigma'_n}{k_n - \frac{\Delta \sigma'_n}{v_m}} \quad (2.3)$$

in which σ'_n is the effective normal stress and V_m is a characteristic volume. Δb is the aperture change and k_n is the stiffness along the normal direction. Evans' model (Evans et al., 1999) is a widely used logarithmic model, as shown in the following equation.

$$\Delta b = - \left(\frac{dk_n}{d\sigma'_n} \right)^{-1} \ln \frac{\sigma'_n}{\sigma'_{ni}} \quad (2.4)$$

where the σ'_{ni} is the reference effective normal stress and k_n is the normal stiffness as defined above.

Rutqvist (1995) used the hyperbolic model to calculate the transmissibility of the fractures, as shown in the following equation.

$$T = C \left[b_{hi} + \frac{\sigma'_{ni}}{K_{ni}} \left(1 - \frac{\sigma'_n}{\sigma'_{ni}} \right) \right]^3 \quad (2.5)$$

where K_{ni} and σ'_{ni} is the reference normal stiffness and reference effective normal stress

respectively. C is an empirical constant. Alm (1999) proposed another equation based on the logarithmic mode.

$$T = C \left[b_{h0} - \left(\frac{dk_n}{d\sigma'_n} \right)^{-1} \ln \frac{\sigma'_n}{\sigma'_{ni}} \right]^3 \quad (2.6)$$

As to the fracture behavior in geothermal reservoirs, Ghassemi and Suresh Kumar (2007) have studied the thermal induced aperture change in a 1-D system. In their work, the aperture change of a single fracture is calculated and compared with analytical solution. Baghbanan and Jing (2007) have investigated the hydraulic properties of fractures in geothermal reservoirs and developed a correlation between hydraulic aperture and fracture length. Berkowitz (1995, 2002) has studied the mechanical behavior using explicitly expressed fracture network model. This work aims to expand the above pioneer research work to get a more practical approach for the simulation of fractured geothermal reservoirs.

2.4 Multi-physics Coupling Strategies

The production of geothermal reservoirs typically involves very complex processes. These processes are thermal, hydraulic or hydrological and mechanical process. The thermal process includes heat flow, such as temperature change, thermal expansion and phase changes. The hydrological process is essentially fluid flow, including transport of components, pressure change and phase distribution. The mechanical process includes stress change and the change of rock properties.

These THM processes are coupled together, which means that the three processes can interact with each other. Such coupling in some cases can be very tight. This can be seen from the following figure.

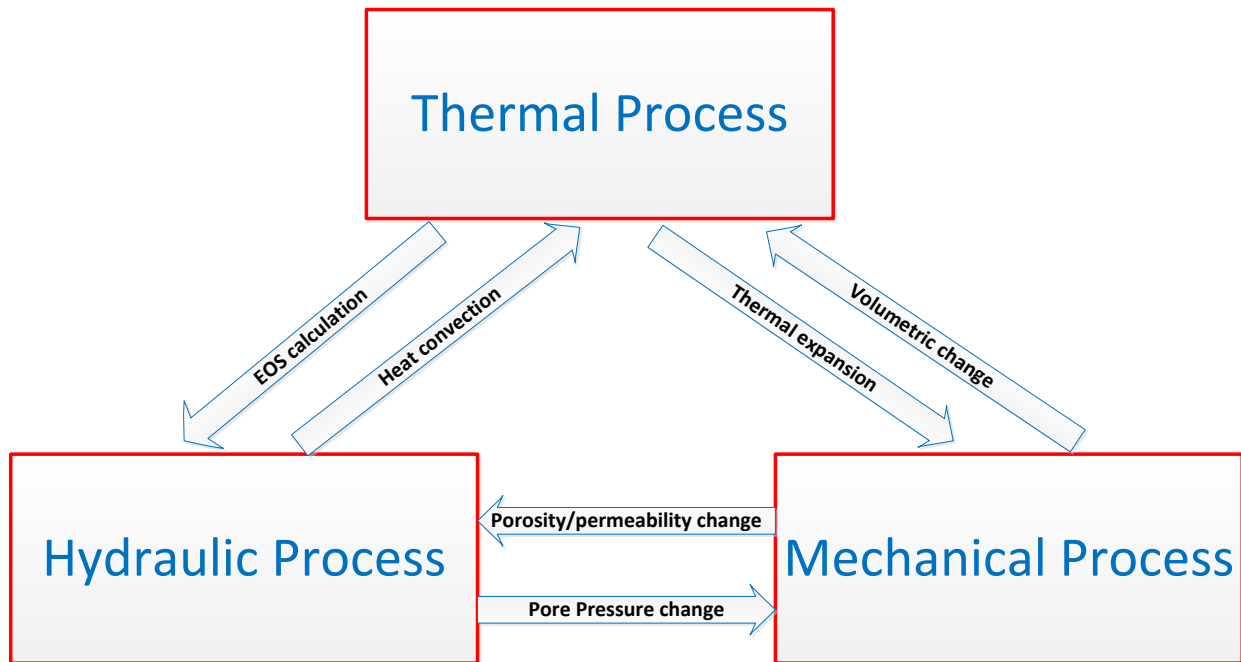


Figure 2-6 Interaction among the THM processes.

As the above figure demonstrates, every pair of processes have influence on each other. For example, the thermal process can affect hydrologic through EOS calculation, while it affects the mechanical process via thermal expansion.

The simulation of above combined processes is a challenge to reservoir simulation. Currently there are three ways to couple these three processes into simulators. Because most THM simulators are actually developed based on a TH or just a hydraulic simulator, the easiest way is to keep the code of the serial simulator untouched, and code a separate mechanical module and couple these two modules sequentially, which is to say that the mechanical module is run after the TH module converges, so that the two modules are run within the same time step. This is called the sequential coupling. Another easy way is to couple the two modules within the same iteration step, known as the iterative coupling. Sequential and iterative coupling are easy to implement, but they suffer from the problem of poor stability, because the partial differential equations are not solved simultaneously. Another drawback of sequential and iterative coupling strategies is that the fluid or energy cannot get converged in such coupling framework. For instance, the stress solved by the mechanical simulation can change the porosity and volume. If the TH equations and the M equation are not solved at the same time, then the porosity and volume used in the TH simulation will be modified in the M equation, therefore the mass and energy conservation cannot be consistent.

Within the THM processes, the mechanical module is especially difficult to couple. So far there are hardly any successful cases. Several researchers have connected reservoir simulators with existing commercial mechanical simulators using sequential or iterative coupling strategy, such as TOUGH-FLAC (Rutqvist, 2011; Rutqvist and Tsang, 2003) and the work based on

UDEC (Kawai, 1979). Such a coupling approach is straightforward. However it is impossible to fully couple two existing simulators together without rewriting the code.

In this work, we propose a mechanical simulation approach, mean stress, to fully couple the THM processes. We have developed a massively parallel fully coupled simulator, THM-EGS. We will use this simulator to simulate the THM behavior of fractured geothermal reservoirs.

2.5 Linear Solver and Multistage Preconditioning

Namely, the multi-stage preconditioning preconditions the linear system in more than one stages. A representative of multi-stage preconditioners is the CPR type preconditioners. The CPR method is firstly proposed by (Wallis, 1983; Wallis. et al., 1985). It has been successfully combined with the Algebraic Multigrid method (Notay, 2010, 2012; Gries et al., 2014), resulting in significant improvement of convergence rate of linear solvers in reservoir simulators.

Basically, finite difference/element method used in reservoir simulation will result in a linear system with mixed characters. For black oil simulation, there typically are three equations within one grid block: one pressure equation and two saturation equations.

The pressure equation solves the oil phase pressure, while the two saturation equations solves the saturation of gas and water respectively. It has been observed that in traditional linear solvers, the two saturation equations converge much faster than the pressure equation. This is because the pressure equation is closer to elliptic partial differential equations, while the saturation equations are closer to parabolic partial differential equations. Therefore, the frequency of the pressure field is much lower than that of the saturation field. For traditional linear solvers, the two types of field are solved using the same algorithm, causing that the components of higher frequency quickly get converged, while the low frequency components converge much more slowly. The

CPR type preconditioners precondition the linear system in two stages. In the first stage, the pressure equation is solved alone with an Algebraic Multigrid linear solver. The result is used to update the residual and variables. In the second stage, the updated residual and variables are substituted into the linear system and the entire linear system is solved with a suitable solver. As such, the low frequent components are eliminated in the first stage when the pressure equation is solved. Therefore, the second stage will be greatly accelerated. On the other hand, only one equation is solved in the first stage, so the size of the linear system is only $1/9$ of the size of the full linear system solved in the second stage. Therefore, the computational load introduced in the first stage is very small.

CHAPTER 3

METHODOLOGY

3.1 Formulation of Fluid and Heat Flow

THM-EGS is a two-phase two-component simulator. The two phases are liquid and gas (vapor) phases, while the two components are air and water components. Each of the two components can exist in either of the two phases. Basically, the governing equations are build based on the mass conservation of components, and the flux term is calculated from phase flow by Darcy's law.

In THM-EGS the governing equations of mass and heat flow are both in general conservation form, as follows.

$$\frac{dM^k}{dt} = \nabla \cdot \vec{F}^k + q^k \quad (3.1)$$

in which k refers mass component or heat. In our simulator, k=1 refers to the water component; k=2 refers to the air component; k=3 refers to the heat 'component'. By integrating the above equation on a representative element volume (REV), we can get the following integrated governing equation

$$\frac{d}{dt} \int_{V_n} M^k dV_n = \int_{\Gamma_n} \vec{F}^k \cdot \vec{n} d\Gamma_n + \int_{V_n} q^k dV_n \quad (3.2)$$

In the above equation, \vec{n} is the normal vector on the surface Γ_n , pointing inward to the REV. On the left side of the above equation, the accumulation term of the fluid equation is

$$M^k = \phi \sum_{\beta} S_{\beta} \rho_{\beta} X_{\beta}^k \quad (3.3)$$

The accumulation term of heat equation can be written in a similar way as follows

$$M^{\kappa} = (1 - \phi) \rho_R C_R T + \phi \sum_{\beta} S_{\beta} \rho_{\beta} u_{\beta} \quad (3.4)$$

The accumulation of heat contains two terms. The first term $(1 - \phi)\rho_R C_R T$ is the energy stored by rock while the second term is the energy stored by fluid. On the right side of Equation (3.1), the mass flux of liquids consists of advection and diffusion, as shown in Equation (3.5)

$$\vec{F}^k = \vec{F}_{adv}^k + \vec{F}_{dif}^k \quad (3.5)$$

The advective flux of a component is the sum over all phases:

$$\vec{F}^k = \sum_{\beta} X_{\beta}^k \vec{F}_{\beta} \quad (3.6)$$

where \vec{F}_{β} is given by the multiphase version of Darcy's law;

$$\vec{F}_{\beta} = -K \frac{K_{r\beta} \rho_{\beta}}{\mu_{\beta}} (\nabla P_{\beta} - \rho_{\beta} \mathbf{g}) \quad (3.7)$$

The diffusive mass flux is given by

$$\vec{F}_{dif}^k = -\phi \tau_0 \sum_{\beta} \tau_{\beta} \rho_{\beta} d_{\beta}^k \nabla X_{\beta}^k \quad (3.8)$$

where the tortuosity, τ_0 , is an intrinsic property of rock matrix while the tortuosity τ_{β} is a property of the fluid. d_{β}^k is the molecular diffusion coefficient for component k in phase β . The heat flow includes conduction and convection:

$$\vec{F}^{k=3} = - \left[(1-\phi)K_R + \phi \sum_{\beta} S_{\beta} K_{\beta} \right] \nabla T + \sum_{\beta} h_{\beta} \vec{F}_{\beta} \quad (3.9)$$

where K_R and K_{β} are properties of the rock and the liquid, respectively, and \vec{F}_{β} is the liquid flow term from Equation (3.5).

3.2 Formulation of Geomechanics Module

Recall that the Hooke's law for isothermal elastic materials is as follows

$$\bar{\tau} = 2G\bar{\varepsilon} + \lambda(\varepsilon_{xx} + \varepsilon_{yy} + \varepsilon_{zz})\bar{I} \quad (3.10)$$

where $\bar{\tau}$ is the stress tensor, $\bar{\varepsilon}$ is the strain tensor, and \bar{I} is a unit tensor.

The above equation has been extended to non-isothermal material by Norris (1992). Later, Norris' thermoelastic version was extended to poro-thermoelastic version with both pressure and temperature effect by McTigue (1986), as shown in Equation (3.11)

$$\sigma_{kk} - (\alpha P + 3\beta K (T - T_{ref})) = \lambda \varepsilon_v + 2G \varepsilon_{kk}, k = x, y, z \quad (3.11)$$

where ε_v is the volumetric strain, as shown in Equation (3.12).

$$\varepsilon_v = \varepsilon_{xx} + \varepsilon_{yy} + \varepsilon_{zz} \quad (3.12)$$

THM-EGS assumes the rock to be linear thermo-poro-elastic material, the behavior of which is subject to Equation (3.11).

For fractured media, the pore pressure and temperature terms are summed over the multiporosity continua. We can see from Equation (3.11) that Lamé's constant represents the effects of uniform strain while the shear modulus represent the effects of directional strain. By summing over the x, y and z component of Equation (3.11) and rewriting it in terms of mean stress and volumetric strain, we get the following equation:

$$\sigma_m - \alpha P - 3\beta K (T - T_{ref}) = \left(\lambda + \frac{2}{3} G \right) \varepsilon_v \quad (3.13)$$

in which

$$\sigma_m = \frac{\sigma_{xx} + \sigma_{yy} + \sigma_{zz}}{3} \quad (3.14)$$

is the mean stress.

Recall the thermo-poro-elastic version of Navier's equation

$$\alpha \nabla P + 3\beta K \nabla T + (\lambda + G) \nabla (\nabla \cdot \vec{u}) + G \nabla^2 \vec{u} + \vec{F} = 0 \quad (3.15)$$

The above Navier's equation has the displacement vector and cross partial derivatives, making it difficult to be solved. We implement divergence to the above equation

$$\alpha \nabla^2 P + 3\beta K \nabla^2 T + (\lambda + 2G) \nabla^2 (\nabla \cdot \vec{u}) + \nabla \cdot \vec{F} = 0 \quad (3.16)$$

in which the divergence of the displacement can be conveniently expressed as the volumetric strain.

$$\nabla \cdot \vec{u} = \varepsilon_v \quad (3.17)$$

From Equation (3.13), the volumetric strain can be expressed by mean stress σ_m . By substituting the expression of volumetric strain into Equation (3.16) and rearranging it, we can get the following equation

$$\frac{3(1-\nu)}{(1+\nu)} \nabla^2 \sigma_m + \nabla \cdot \vec{F} = \frac{2(1-2\nu)}{(1+\nu)} (\alpha \nabla^2 P + 3\beta K \nabla^2 T) \quad (3.18)$$

The above equation is the governing equation of mechanical simulation for single-continuum in THM-EGS.

Besides single-continuum porous media, THM-EGS is also capable of calculating the mechanical response of fractured-matrix system (multiple continua system). In this simulator, the Multiple Interacting Continua (MINC) approach is extended to simulate fracture and matrix interactions with mechanical effect. The details of MINC can be found in Pruess and Narasimhan (1985) and Wu and Pruess (1988). Basically, in MINC approach the complex fracture-matrix system is treated as multiple continua. Adjacent continua interact with each other. The thermo-poroelastic version of Hook's law for the j th continuum in the MINC system is derived by Winterfeld and Wu (2014) as

$$\sigma_{kk} - \left[\sum_j (\alpha_j P_j + 3\beta K w_j (T - T_{ref})) \right] = \lambda \varepsilon_v + 2G \varepsilon_{kk}, k = x, y, z \quad (3.19)$$

in which α_j is the generalized Biot's coefficient introduced by Wilson and Aifantis (1982).

w_j is the volume fraction of the j th continuum.

Here each continuum has its unique pore pressure and temperature, meanwhile all continua share the same stress and strain. The relationship among the modulus is as follows.

$$E = 2G(1 + \nu) \quad (3.20)$$

$$E = 3K(1 - 2\nu) \quad (3.21)$$

$$\lambda = \frac{2\nu G}{1 - 2\nu} \quad (3.22)$$

Based on the above extended Hook's law, with a similar derivation as that of the single-continuum version, the governing geomechanical equation of MINC model can be derived as

$$\frac{3(1-\nu)}{(1+\nu)} \nabla^2 \sigma_m + \nabla \cdot \bar{F} = \frac{2(1-2\nu)}{(1+\nu)} \sum_{i=1}^N (\alpha_i \nabla^2 P_i + 3\beta_i K \nabla^2 T_i) \quad (3.23)$$

where i denotes a certain block of continua and N is the total number of blocks in each MINC set.

3.3 Fluid Properties

The fluid properties of the water phase and the vapor phase, including the relative permeability, the viscosity and the density, are calculated in the EOS module. The fluid properties in THM-EGS is primarily based on the NIST Standard Reference Databases (Lemmon et al., 2005). As most of the property correlations do not have explicit formulation, we plot the value as the function of pressure and temperature in Appendix A and Appendix B.

3.4 Mechanical Properties

As mentioned, the mechanical properties of materials will be changed subject to the variations of hydro-thermal field. The mechanical property correlations of material used in THM-EGS are as follows.

In this work, the mechanical properties of matrix rock and fractures are treated differently. The porosity of the matrix rock is calculated as

$$\phi = \phi_0 \left(1 + c_p (P - P_{ref}) + 3\beta (T - T_{ref}) \right) \quad (3.24)$$

where c_p is the pore compressibility and β is the thermal expansion coefficient. P_{ref} and T_{ref} is the reference pressure and reference temperature respectively.

The matrix permeability is calculated using Carman-Kozeny equation as

$$K = K_0 \left(\frac{1 - \phi_0}{1 - \phi} \right)^3 \left(\frac{\phi}{\phi_0} \right)^3 \quad (3.25)$$

The porosity of the fracture is calculated by the following equation

$$\phi = \phi_0 \frac{b_1 + b_2 + b_3}{b_{1,0} + b_{2,0} + b_{3,0}} \quad (3.26)$$

where b_i is the updated fracture aperture in the i th direction and b_{i0} is the referential fracture aperture in the i th direction.

The fracture permeability is calculated based on the cubic law

$$K_{fi} = \frac{b_i^3}{12L_i} \quad (3.27)$$

where K_{fi} is the fracture permeability in the i th direction and L_i is the fracture spacing in the i th direction.

The fracture aperture is the function of pressure, temperature and stress. Therefore the fracture aperture will be changed during the production process and the fracture properties are coupled in the simulation in this way. The approach to capture the fracture aperture change will be proposed in the next chapter.

The change of pore diameter will induce the change of capillary pressure. For both fracture and matrix blocks, as porosity and permeability change, capillary pressure also changes, as shown in the following equation

$$P_c = P_{c0} \sqrt{(K/\phi)_0} / \sqrt{(K/\phi)} \quad (3.28)$$

where P_{c0} is the capillary pressure calculated from current gas saturation. The volumetric strain changes the volume of a certain block is

$$V = V_0 (1 - \varepsilon_v) \quad (3.29)$$

3.5 Numerical Approach

We use Integral Finite Difference (IFD) method to solve the above governing equations, e.g. Narasimhan and Witherspoon (1976); Celia et al. (1990). Using the IFD method, the governing equations are discretized as the following general form

$$\frac{(V^{i+1} M^{k,i+1} - V^i M^{k,i})}{\Delta t} = \sum_m A_{nm} F_{nm}^k + q^k \quad (3.30)$$

In the above equation, i denotes a certain time step, m denotes a certain connection between two neighboring blocks, and n denotes a certain weighting scheme. The above nonlinear equations are solved by the Newton-Raphson method.

The above equation is the integral of the governing equation on a representative elementary volume (REV) (Pruess et al., 1999). Therefore, instead of calculating the discretized finite difference, IFD calculates the flux of fluid/energy flow on the interface between each pair of connected REVs and the accumulated fluid/energy in each REV.

Compared to the traditional finite difference method, IFD method is more flexible in the simulation of unstructured grids. Meanwhile, as the IFD method is fully based on a connection list, it is more convenient to use. Actually, with this method, the users only need to input a

connection list of the graph with the volume of each block and the interface area of each connection specified. A detailed description of IFD method and the numerical approach can be found in Narasimhan and Witherspoon (1976).

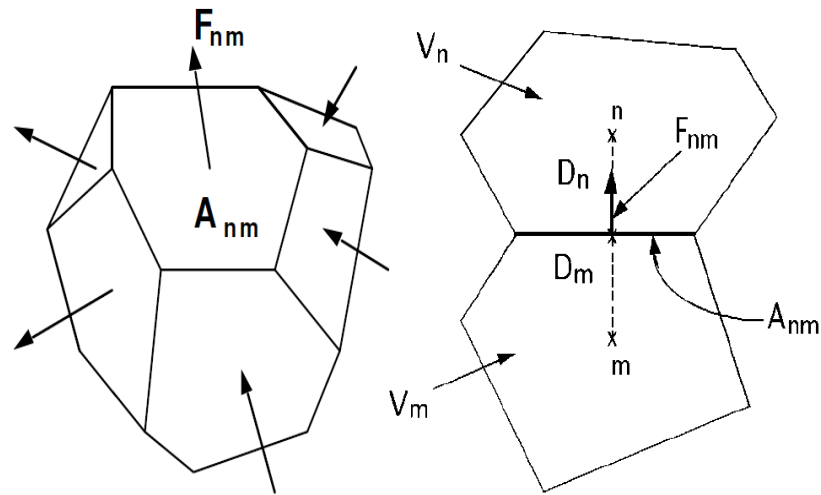


Figure 3-1 Integral finite difference method on REV (Pruess et al., 1999).

CHAPTER 4

SEMI-ANALYTICAL ANALYSIS OF FRACTURE APERTURE

4.1 Limitations of Existing Fracture Aperture Models

As mentioned in the introduction session, several models for calculating fracture aperture change have been developed, including the hyperbolic model and the logarithmic model. The existing models have been widely used in commercial reservoir simulators and have shown their feasibility. However, these models have several limitations. At the first place, most of them are empirical correlations based on uniaxial experimental results with certain fitting parameters. It has been observed that there is scale effect between the fractures in drill core and in situ condition, as shown in the following Figure 4-1. The figure shows that the normal closure predicted by the drill core test is significantly different from the in situ normal closure. Secondly, thermal process is not considered in the existing models. Thirdly, the normal effective stress cannot be computed by the mean stress approach. Actually, it is always difficult to exactly capture the normal effective stress on the matrix-fracture.

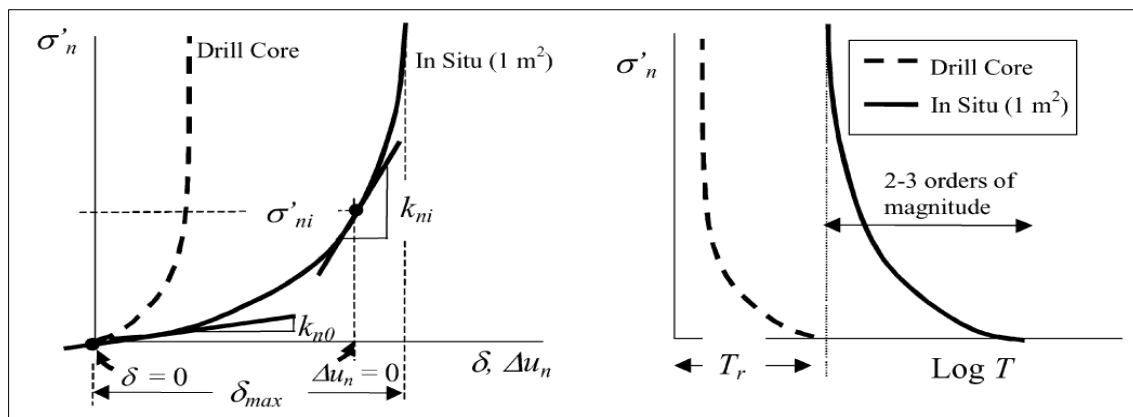


Figure 4-1 Scale effect of mechanical normal closure (Rutqvist et al., 2003).

4.2 Derivation of the Correlation

In this work, a semi-analytical fracture aperture correlation is developed. The method is essentially analogous to Warren and Root's way of calculating the shape factor of fractures (Warren and Root, 1963).

Consider a matrix block surrounded by fractures of length L_i on the i th direction, as shown in Figure 4-2. Analogous to the derivation of shape factor of Aziz (Lim and Aziz, 1989), the temperature and pressure in the fractures are kept to be constant, respectively P_f and T_f . The initial temperature and pressure of the matrix block is P_{m0} and T_{m0} .

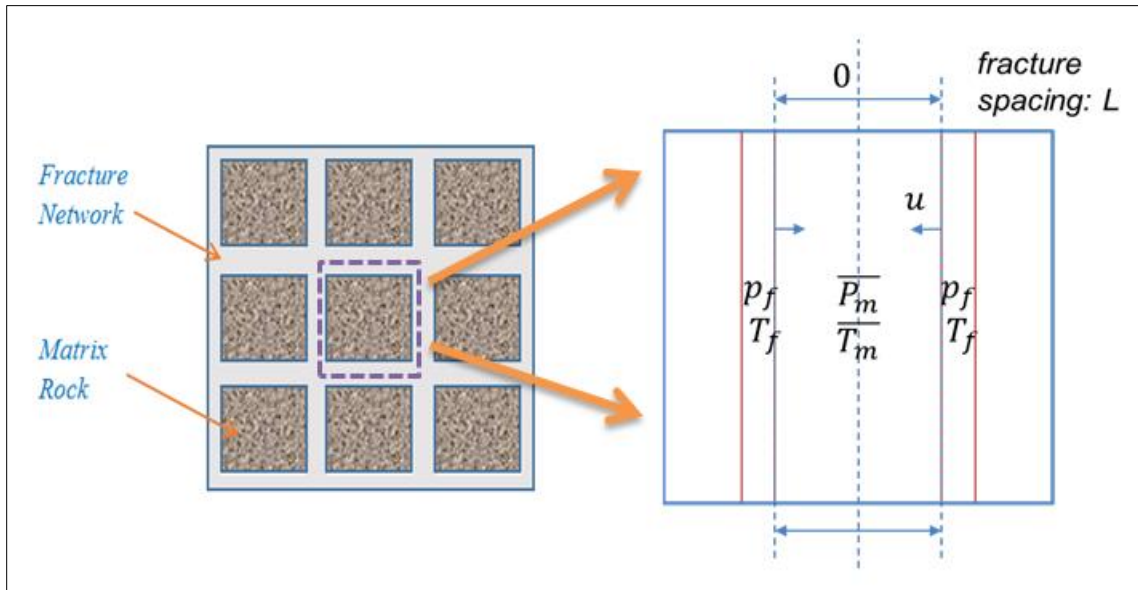


Figure 4-2 Conceptual model of fracture surrounded matrix block.

If the matrix permeability is low enough, which is the case of HDR and certain unconventional resources, the heat convection in the matrix is not comparable to the heat conduction. Therefore, the leak off effect can be neglected without a fundamental change of the final results.

In a Cartesian coordinate, the 1-D version of the governing displacement equation of the matrix rock without leak-off term can be reduced to

$$\frac{\partial u^2}{\partial x^2} = \frac{1+\nu}{1-\nu} \beta \frac{\partial(T-T_{m,0})}{\partial x} \quad (4.1)$$

with the boundary condition on the center of the matrix block (Eslami et al. 2013)

$$u_x(x = 0, t) = 0 \quad (4.2)$$

The above equation can be solved with a general solution as

$$u_x = \frac{1+\nu}{1-\nu} \beta \int_0^x (T - T_{m,0}) dx + Cx \quad (4.3)$$

in which C is a constant to be determined. The change of normal stress inside the matrix block can be calculated from displacement using Equation (3.11)

$$\Delta\sigma_{xx} = \frac{E_m}{(1+\nu)(1-2\nu)} \left[(1-\nu) \frac{\partial u_x}{\partial x} - (1+\nu) \beta (T - T_{m,0}) \right] \quad (4.4)$$

Note here the above equation is based on the assumption of uni-axial compaction, so that the volumetric strain is just equal to the normal strain along the x direction.

The boundary condition on the matrix-fracture interface is essentially a force balance condition, as shown in the following equation

$$\Delta\sigma_{xx}(L/2) = -k_f u \left(\frac{L}{2} \right) - \Delta P_f \quad (4.5)$$

where P_f is the pressure in the fracture and k_f is the mechanical stiffness of the fracture. Here the fracture is treated as a linear spring and $-k_f u(L/2)$ is the resistance force of the fractured material. Note that the temperature and pressure gradient at the fracture-matrix interface is typically perpendicular to the fracture plane, therefore the above assumption is reasonable. If the fracture is treated as vacant, then k_f is zero. Note that since the displacement points inward, there

should be a negative sign in front of the resistance force. The conceptual model of fracture resistance is shown in the following figure.

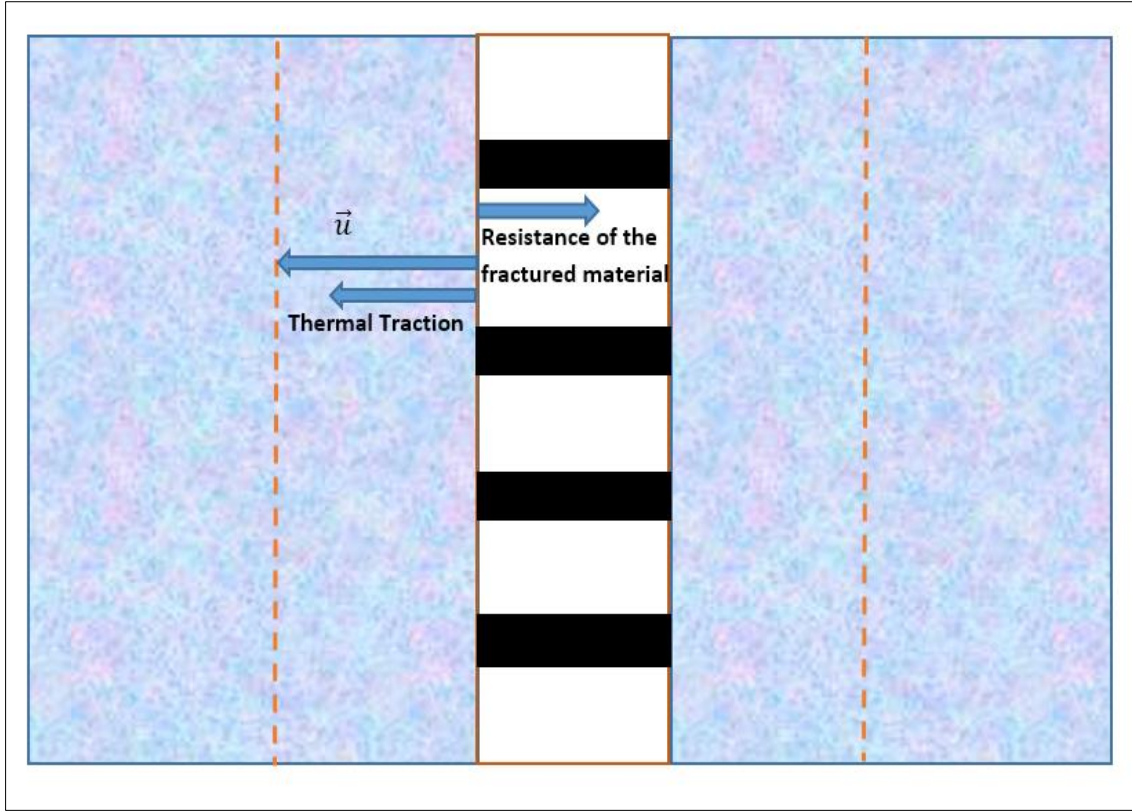


Figure 4-3 Conceptual model of fracture resistance.

As to the integral, using the concept of dual continuum, we can get

$$\int_0^x (T - T_{m,0}) dx = \frac{1}{3} \frac{L_i}{2} (\bar{T}_m - T_{m,0}) \quad (4.6)$$

By substituting the formulation of the normal stress at the matrix-fracture interface into the boundary condition, we can solve the constant C as

$$C = \frac{-(P_f - P_{f,0}) + \frac{1}{3} \beta (\bar{T}_m - T_{m,0}) \frac{2E_m}{1-2\nu} - \frac{1}{3} k_f \frac{1+\nu}{1-\nu} (\bar{T}_m - T_{m,0}) L_i / 2}{\frac{E_m}{1-2\nu} + k_f L_i / 2} \quad (4.7)$$

Note that here k_f is treated as a constant value. It can also be a function of the displacement of fracture-matrix interface, as

$$k_f = k_f \left(u \left(\frac{L}{2} \right) \right) \quad (4.8)$$

Then C may not be expressed explicitly and should be solved iteratively.

Under the assumption of constant fracture stiffness, the displacement at matrix-fracture interface is

$$u_i = \frac{-(P_f - P_{f,0}) + \beta(\bar{T}_m - T_{m,0}) \frac{E_m}{1-2\nu} \cdot \frac{L_i}{2}}{\frac{E_m}{1-2\nu} + k_f L_i / 2} \quad (4.9)$$

The fracture aperture change is two times the absolute value of fracture-matrix interface displacement

$$\Delta b_i = -2\Delta u_i \left(\frac{L_i}{2} \right) \quad (4.10)$$

Then the fracture aperture change can be expressed as

$$\Delta b_i = \frac{(P_f - P_{f,0}) - \beta(\bar{T}_m - T_{m,0}) \frac{E_m}{1-2\nu} \cdot L_i}{\frac{E_m}{1-2\nu} + k_f L_i / 2} \quad (4.11)$$

where b_{i0} is the initial aperture of the fracture along the i th direction.

The fracture permeability can be calculated by cubic law as

$$K_i = C_i \frac{(b_{i0} + \Delta b_i)^3}{12L_i} \quad (4.12)$$

where C_i is a parameter to correlate between the mechanical aperture and the hydraulic aperture.

Many researchers in civil engineering (Witherspoon et al. 1979, 1980; Renshaw et al., 1995;

Cappa et al., 2005) have investigated the relationship between the mechanical aperture b_m and the hydraulic aperture b_h , as shown in Fig 4-4 on page 27.

From the above figure, we can see that when aperture is greater than 10^{-5} m ($10 \mu\text{m}$), the mechanical aperture and hydraulic aperture are almost the same. This is easy to understand, because as fracture aperture increases, the flow channel inside the fracture becomes wider, so

that the effect of fracture surface tends to be less and less. In this work, all fracture apertures exceed $10\mu\text{m}$, therefore C_i is set to be 1.

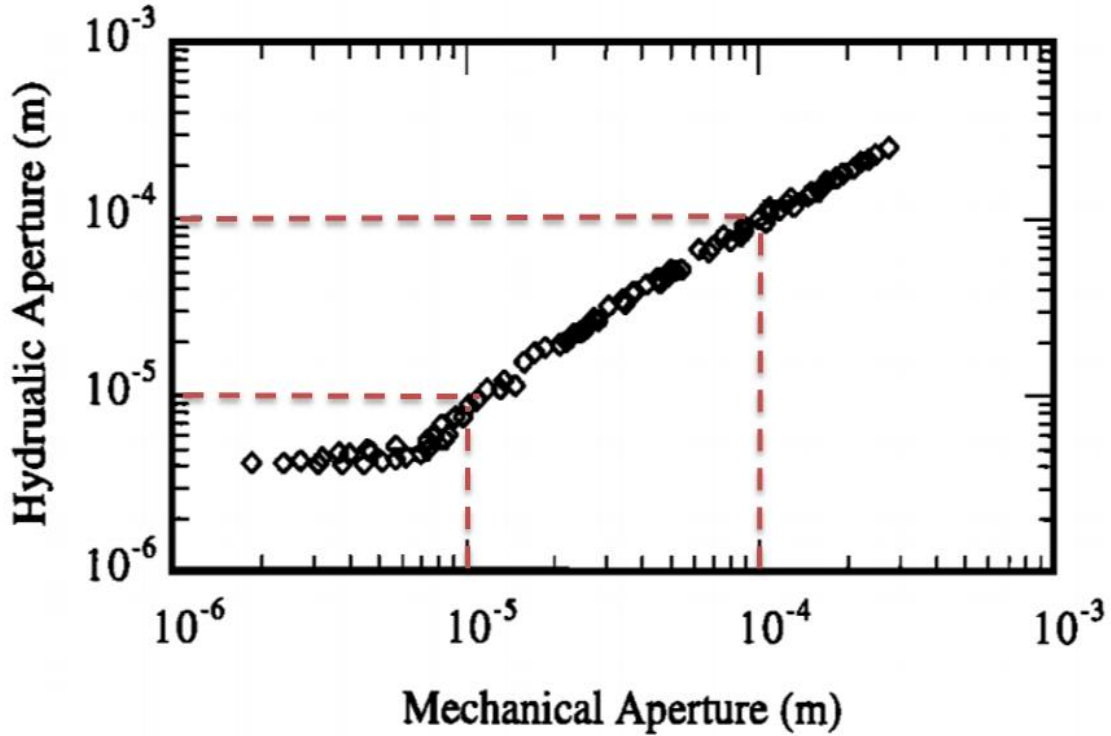


Figure 4-4 Relationship between mechanical aperture and hydraulic aperture (Witherspoon et al., 1980).

Compared to the existing correlations, this newly developed correlation has several advantages. Firstly, the new correlation is based on analytical derivation. The formulation can reflect more physics. Secondly, the new correlation quantifies the hydraulic effect and thermal effect respectively, so that it helps researchers better understand the aperture change process. Thirdly, the new correlation is based on the concept of dual continuum that is used in reservoir simulators. Therefore, it can be used not only in discrete fracture network (DFN) simulation, but also in dual continuum simulation. Fourthly, the new correlation doesn't explicitly contain the effective normal stress term, so that it can be easily implemented into existing reservoir simulators that are without a mechanical simulation module. Fifthly, the correlation can be also

applied to fractures with combined elastic-plastic behavior, even if the mechanical module is based on elastic assumption.

4.3 Sensitivity Analysis and Elastic-Plastic Extension

We use analytical solutions to verify the proposed correlation. In 1-D system, if the leak-off effect is ignored, the thermal governing equation in the matrix can be reduced to

$$(1-\phi)K\nabla^2 T_m = (1-\phi)\rho_R C_R \frac{\partial T_m}{\partial t} \quad (4.13)$$

By implementing the boundary and initial conditions

$$T_m(x=0, t) = T_f \quad (4.14)$$

$$T_m(0 < x < L, t=0) = T_{ini} \quad (4.15)$$

The governing equation can be solved as

$$T_m = T_f + \sum_{n=1}^{\infty} \frac{4(T_{ini} - T_f)}{(2n-1)\pi} \sin\left[\frac{(2n-1)\pi}{L}x\right] e^{-\frac{K}{\rho_R C_R} \frac{(2n-1)^2 \pi^2}{L^2} t} \quad (4.16)$$

The matrix temperature at the center ($x=L/2$) is

$$T_m\left(\frac{L}{2}\right) = T_f + \sum_{n=1}^{\infty} \frac{4(T_{ini} - T_f)}{(2n-1)\pi} \sin\left[\frac{(2n-1)\pi}{2}\right] e^{-\frac{K}{\rho_R C_R} \frac{(2n-1)^2 \pi^2}{L^2} t} \quad (4.17)$$

The average temperature of matrix rock \overline{T}_m is

$$\overline{T}_m = \frac{\int_0^L T_m dx}{L} = T_f + \sum_{n=1}^{\infty} \frac{8(T_{ini} - T_f)}{(2n-1)^2 \pi^2} e^{-\frac{K}{\rho_R C_R} \frac{(2n-1)^2 \pi^2}{L^2} t} \quad (4.18)$$

We choose the following parameters

Table 4-1 parameters for calculating matrix temperature and aperture change

Properties	Values	Units
Young's modulus	66.0	GPa
Fracture spacing	0.3	m
Poisson's ratio	0.25	dimensionless
Biot's coefficient	1.0	dimensionless
Linear thermal expansion coefficient	7.9	10^{-6} m/(m K)
Thermal conductivity of dry rock	1.0	W/(m K)
Heat capacity of rock	1000	J/ (kg K)
Initial temperature of matrix	220	°C
Fracture temperature	80	°C
Density of rock	2.5	103 kg/m ³

By substituting the above parameters into the formulations, we can plot $T_m(L/2)$ and \bar{T}_m is in Figure 4-5 on page 30.

The fracture aperture change is plotted in Figure 4-6 on page 30. As we can see, the fracture aperture will rapidly increase within one hour. As shown by Figure 4-7 on page 31, the fracture aperture is sensitive to the thermal expansion coefficient of the matrix. The sensitivity analysis with respect to other properties will be shown in Chapter 7.

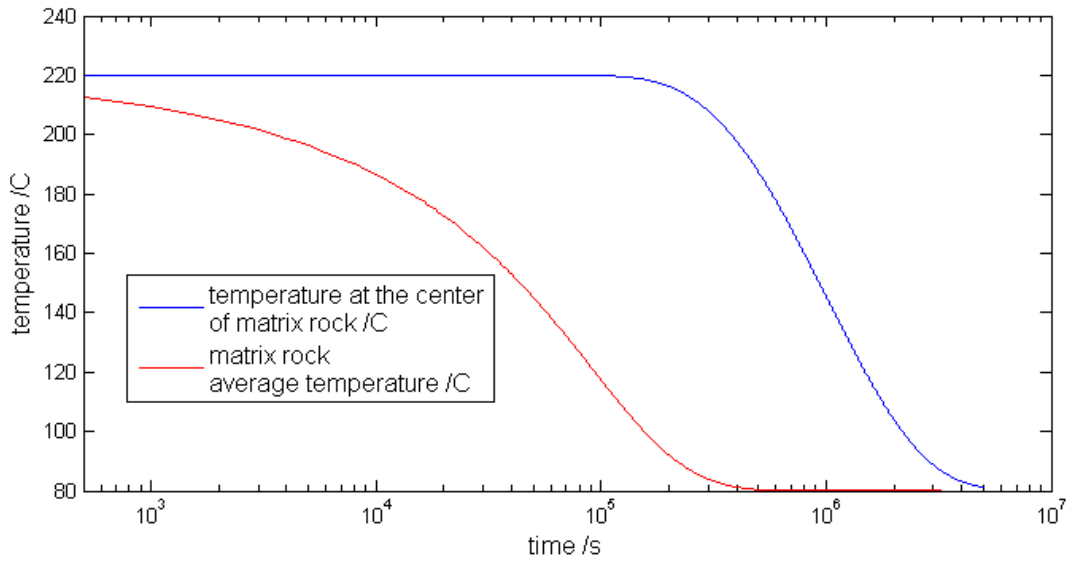


Figure 4-5 Comparison between average matrix temperature and the temperature at the center of the matrix rock.

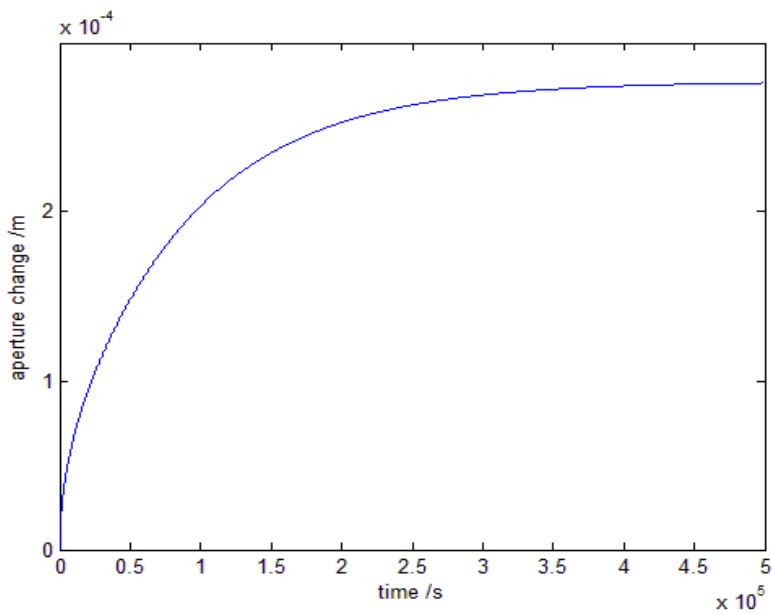


Figure 4-6 Fracture aperture change versus time.

The correlation can be also applied to cases where the fractures have elastic-plastic resistance. If the fracture is treated as elastic-plastic material, then the fracture has different stiffness within elastic and plastic zone. When deformation is relatively small, the fracture has elastic behaviors with constant elastic stiffness. The fracture resistance transit into plastic material, when the

entire the fracture aperture change exceed a certain ‘breaking’ criteria. For example, we assume the deformation at which fracture breaks is 1 mm. Within the elastic zone, the resistance of the fracture is set to be 16 GPa/m. Within the plastic zone, the resistance of the fracture is set to be 1 GPa/m, as shown in Fig 4-8.

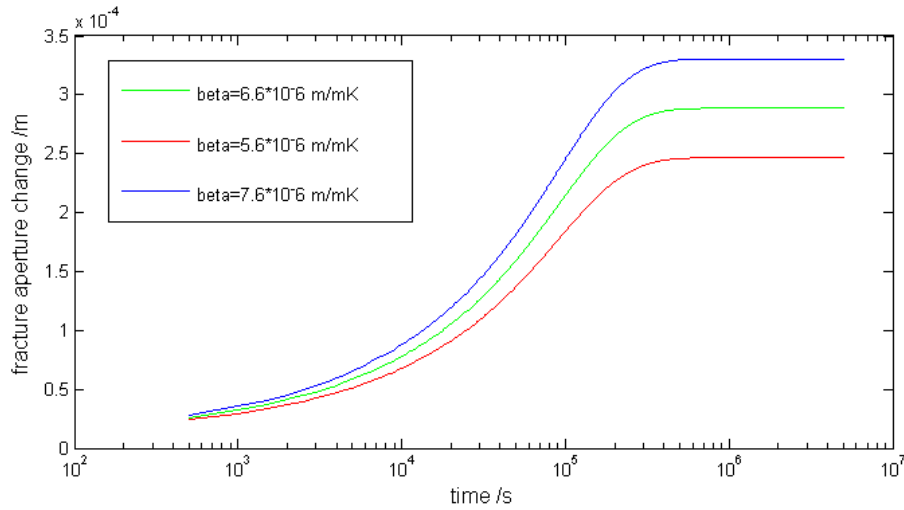


Figure 4-7 Fracture aperture change versus time with different thermal expansion coefficients.

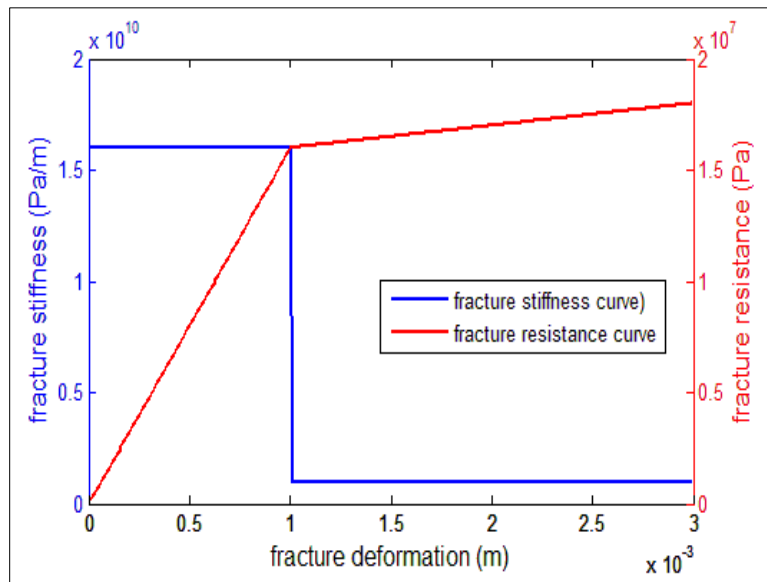


Figure 4-8 Elastic-plastic deformation of fracture. Blue line: fracture stiffness curve. Red line: fracture resistance curve.

We assume the rock properties are the same as the previous cases but set the injection temperature to be 20 °C, approximately the atmosphere temperature. As the injection temperature is lowered, the fracture aperture change may exceed the elastic zone, causing the plastic deformation, as shown in the following figure.

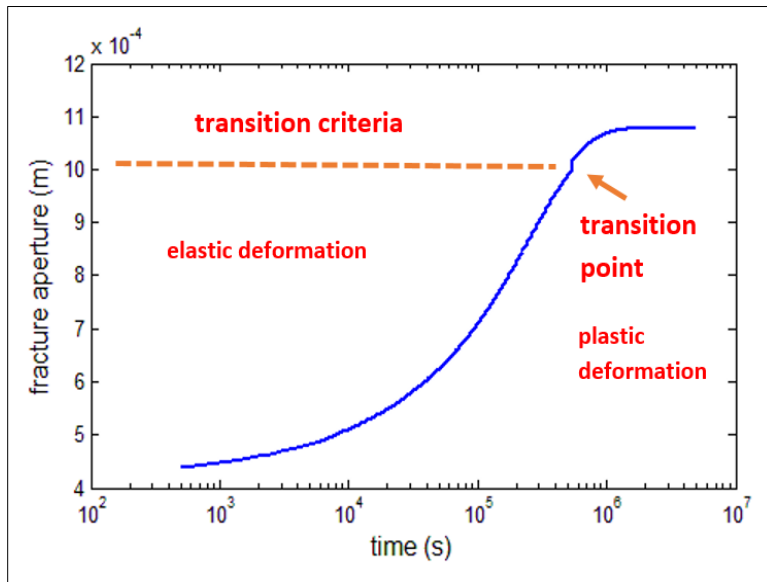


Figure 4-9 Fracture aperture with elastic-plastic resistance. The arrow indicate the transition point from elastic deformation region to plastic deformation region.

As demonstrated by the above figure, the fracture aperture will exceed 1mm criteria if the injection temperature is low enough. Therefore, if the EGS fractures are closed after hydraulic fracturing, the operator can stop the water recycling and inject colder water with atmosphere temperature to create a larger stress on the fracture-matrix interface, then the closed fractures might get reactivated.

CHAPTER 5

SIMULATOR DEVELOPMENT AND VERIFICATION

In this work, a fully coupled thermal-hydraulic-mechanical geothermal reservoir, called THM-EGS has been developed. In this chapter, we present the design and verification cases of THM-EGS.

THM-EGS is based on an extensible framework that is specially designed for multi-physics coupling. THM-EGS is a next generation reservoir simulation platform. It is an object-oriented parallel software written in FORTRAN03. THM-EGS has a general Integral-Finite-Difference (IFD) framework. The parallel part of THM-EGS is written with hybrid MPI/OPENMP language, which enables communication between processors. With the hybrid MPI/OPENMP parallel framework, THM-EGS is able to conduct large scale simulation with millions of grid blocks on clusters.

5.1 Fully Coupled Multi-Physics Coupling Framework

Multi-physics coupling has gradually become the main stream of scientific computation. A comprehensive review of the state-of-the-art of coupling techniques can be found in Keyes (2013). Although several multi-physical simulators have been developed, very few of them are fully coupled simulators. THM-EGS adopts an object-oriented data structure for coupling different physical processors. In THM-EGS, element-based data and connection-based data are all stored in data types, so that the required data are packed up. Such design makes the simulator more extensible, so that the simulator can be modified for more general purposes.

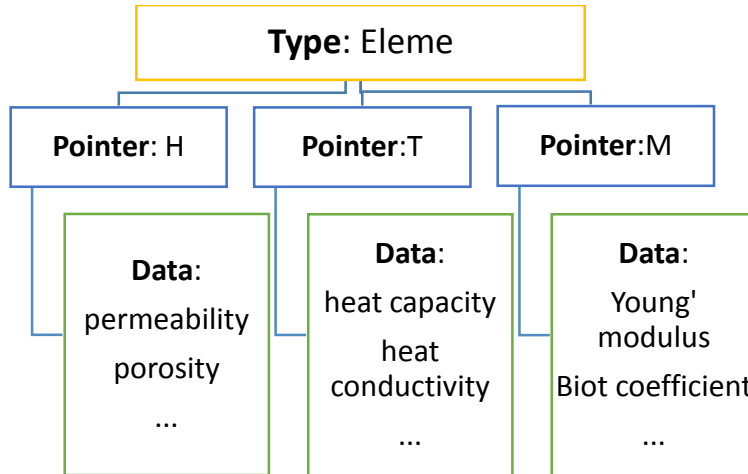


Figure 5-1 Data structure of element-based data types.

5.2 Equation-of-state (EOS) module and primary variables

To calculate the properties of gas-liquid system, THM-EGS has a two-phase two-component EOS module, in which the gas phase is treated as real gas with the Z factor input from a table in the input file.

The choice of primary variables is as follows. For each grid block, the first, third and fourth primary variable is always gas pressure, temperature and stress respectively, while the second primary variable varies for different phase condition. For single phase condition, the second primary variable is the air mass fraction in the present phase, while for double phase condition, the second primary variable is chosen as the gas phase saturation. As such, when one phase disappear or re-appear in one grid block, the primary variables of that grid block are changed accordingly.

In THM-EGS, after one iteration, the primary variables of each grid block are updated and the new value is used to check whether the phase condition is going to change. THM-EGS adopts a subroutine *Phase_Checker* to conduct this operation. *Phase_Checker* is called at the

beginning of each iteration. In *Phase_Checker*, all grid blocks are looped through and the saturation pressure of water in that grid block is calculated as a function of temperature,

$$P_{sat} = P_{sat}(T) \quad (5.1)$$

Once the saturation pressure is calculated, the value is used to determine the phase condition. If the saturation pressure is larger than the gas phase pressure, it means that the gas phase cannot support the air component, therefore gas phase should disappear and the two-phase system switch to single phase system.

THM-EGS uses a 'phase flag' to denote the phase condition of a certain grid block. Once a phase is found to disappear or re-appear in the grid block, the phase flag is then updated accordingly and the primary variables of that grid block are also changed. For instance, if the previous system is gas phase and liquid phase appears in the updated system, then the second primary variable of this grid block is set as gas saturation and the value of gas saturation is set to be a small number according to the floating-point accuracy of the computer system.

5.3 Parallel framework

The parallel framework of THM-EGS consists of two parts: the parallel preprocessing part and the parallel simulation part.

5.3.1 Parallel Preprocessing

THM-EGS adopts domain decomposition approach to solve the fully-coupled nonlinear system, in which each processor is assigned with a subdomain of the whole reservoir. As such, a parallel preprocessing module is needed to process input data and distribute work.

In THM-EGS, a master-slave framework is used in which a randomly chosen processor, called the master processor, reads the input file, sets up the global mesh, calls METIS to do graph partition, and distributes local versions of information to every processor. From the master

processor, the other processors, named slave processors, receives their local version of connection list, pointers of the Jacobian matrix, and initial conditions. In this process, the master processor has to store some global versions of arrays, such as the permeability of all elements, which may take huge amounts of memory. To optimize memory usage, the above operations are conducted one at a time so that the master processor will not store many global arrays at the same time. A detailed flowchart of this preprocessing framework is shown in Figure 5-2.

The advantage of the master-slave framework is that it is simple and easy to implement. A drawback of this framework is that it is not scalable. But as the CPU time spent in preprocessing is only a small portion of the total simulation time, the loss of scalability is negligible in most cases. Another possible drawback of the master-slave framework is that, the input job is done by the master processor. The user-provided element-based initial condition requires result huge memory consumption on the master processor. To minimize this problem, THM-EGS distributes the data immediately after one type of initial condition is read in, instead of distributing all the initial conditions after the end of input.

The parallel part of THM-EGS is also object-oriented, with the MPI derived data type widely used in the simulator. The MPI derived data type is used to store the rock type data and the element-based initial conditions for different physical module. The MPI derived data type has two advantages. Firstly, it reduces the amount of parallel communication, which is more much expensive than calculation. The MPI derived data type packs up different types of data and communicate them at one single time, so that much simulation time can be saved. Secondly, with the MPI derived data type, the code becomes much easier to modify. Using the MPI derived data type, other developers can add new simulation features into the simulator without working

much on the parallel code. Actually, developers only need to change the way that the MPI derived data type is constructed, but keep the parallel framework as it is.

To partition the whole reservoir domain, THM-EGS uses the METIS package, which is a widely used graph partitioning tool. A detailed technique description of METIS can be found in the work of Karypis and Kumar (1995). METIS requires the graph to be stored in the adjacency list format. METIS partitions the reservoir into several overlapping subdomains. The inner part of a subdomain is called the UPDATE part, while the border of the subdomain is called the EXTERNAL part. As such, the EXTERNAL part of a certain subdomain is located in the UPDATE part of one of its neighboring subdomains. In this thesis, such elements are called the overlapping elements.

To sum up, compared to the previous parallel preprocessing framework, the new framework helps boost up the efficiency of memory usage and communication among processors. The object-oriented nature of the new framework maintains the high extendibility of the code.

The new framework can be easily changed from the previous one, by simply rearranging the sequence of existing subroutines and writing a few new subroutines for the construction of derived data types.

5.3.2 Parallel Simulation

For the parallel simulation part of the framework, in each iteration step each processor builds its local part (UPDATE) of the Jacobian matrix and residual array. After the Jacobian matrix is built, the AZTEC package, e.g. Tuminaro et al. (1999), the iterative linear solver, is called simultaneously by all the processors to solve the linear system, e.g. Wu et al. (2002).

AZETEC gives back the increments of the primary variables of the UPDATE part to its processor. After each iteration, increments of the primary variables of the overlapping elements are exchanged between neighboring processors and each processor updates the secondary variables on both UPDATE and EXTERNAL parts of its subdomain. As such, the secondary variables on the border are calculated repeatedly by neighboring processors. The purpose of such treatment is to reduce the amount of communication among processors, which is far more expensive than computation.

To avoid processor conflicts, all the output job is carried out by the master processor. As such, after each time step, all processors send their information back to the master processor, in order to generate printout file.

In summary, input/output and distribution of work is carried out by the master processor, while all time-consuming work, including assembling the Jacobian matrix and solving linear system, is done by all processors in parallel. A detailed parallel simulation flowchart is shown in Figure 5-3.

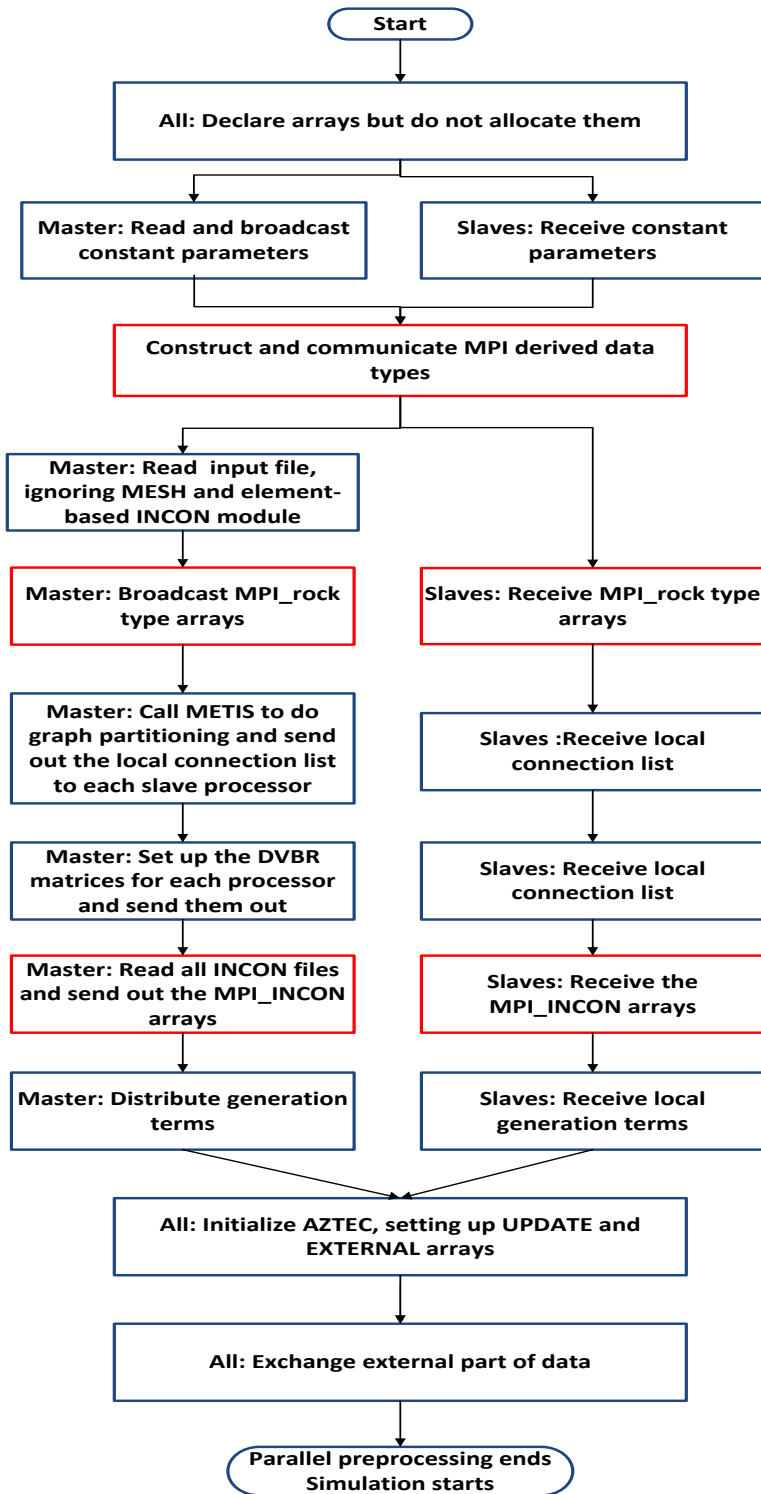


Figure 5-2 Flowchart of parallel preprocessing part of the simulator. Red parts indicates the MPI derived data type for element-based initial condition.

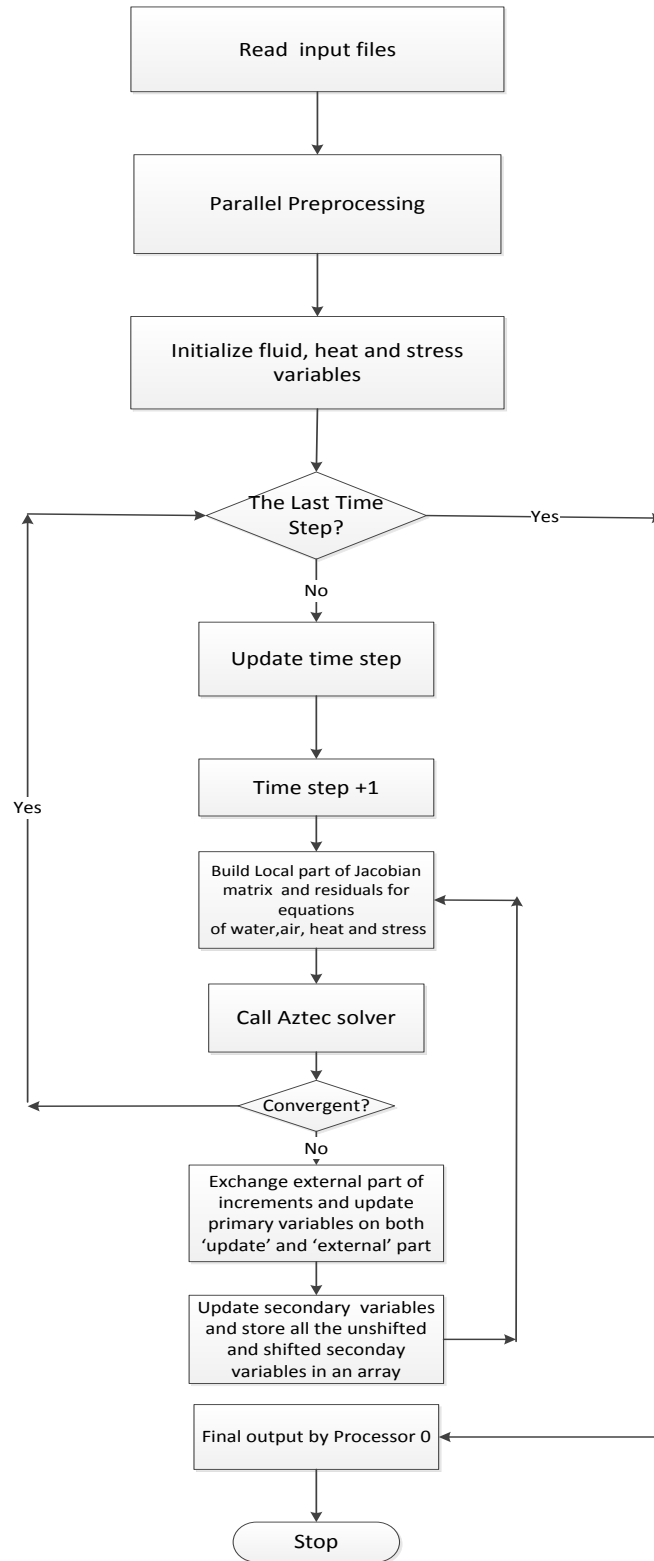


Figure 5-3 Flow chart of the whole simulator.

5.3.3 Parallel Jacobian Construction and Optimized Memory Storage

THM-EGS constructs the Jacobian matrix in a way that is similar to that of MSFLOW, a multiphase simulator developed by Wu (1998). In MSFLOW, for each element, all of its neighbors are looped and the derivatives are calculated. In this way, the Jacobian is built column by column, so that the memory can be significantly saved. THM-EGS parallelized the above framework. The main advance in the new framework, the ‘unshifted’ flux is record and reused for the calculation of derivatives. In this way, the computational loads is reduced to the level of that of TOUGH2. Meanwhile, shifting and calculation is still based on element, so that the memory usage of the new framework is still efficient enough to handle large problems.

5.4 Simulator Verification

In this section, we present two verification cases to show the accuracy and parallel performance of THM-EGS.

5.4.1 2-Dimensional Compaction with Mandel-Cryer Effect

In this example, we use our simulator to solve the two dimensional compaction problem. Given a piece of saturated poroelastic material, a constant compressive force is applied on the top, compressing the material and causing the pore pressure inside to increase. Afterwards, the material is allowed to drain on the lateral direction. The drainage occurs on the edges and leads to the decrease of pore pressure there, causing some additional load to be transferred to the center of the material. The pore pressure in the center will continue to increase until it reaches a maximum and then declines. This effect was firstly studied by Mandel (1953) and is called the Mandel-Cryer effect. Later, Abousleiman et al. (1996) presented an analytical solution to this problem. Figure 5-4 shows its configuration.

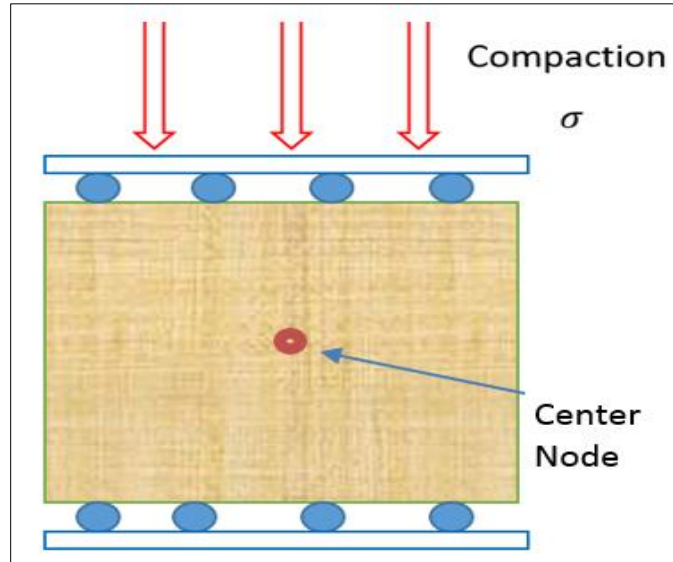


Figure 5-4 Problem description of 2-dimensional compaction.

In this work, we study the Mandel-Cryer effects under different permeability conditions.

Case #1 has a higher permeability and case #2 has a lower permeability.

Table 5-1 Input parameters for 2-D compaction cases

Properties	Values	Units
Permeability of case #1	$K_x=K_z=3.0 \cdot 10^{-13}$	m^2
Permeability of case #2	$K_x=K_z=1.0 \cdot 10^{-15}$	m^2
Porosity	0.15	dimensionless
Young's modulus	15.0	GPa
Poisson's ratio	0.3	Dimensionless
Biot's coefficient	1.0	dimensionless
Water viscosity	0.001	Pa·S

For both cases, the material is discretized into $20 \times 24 = 480$ grid blocks with uniform size. The problem is solved by a PC work station. The PC has an Intel Core i7 processor with 16 processors and 32 Gigabytes of memory. The simulation is run by 4, 8 and 16 processors. The partitioned graph of the case of 8 processors is shown in Figure 5-5, from which we can see that METIS roughly partitions the graph evenly.

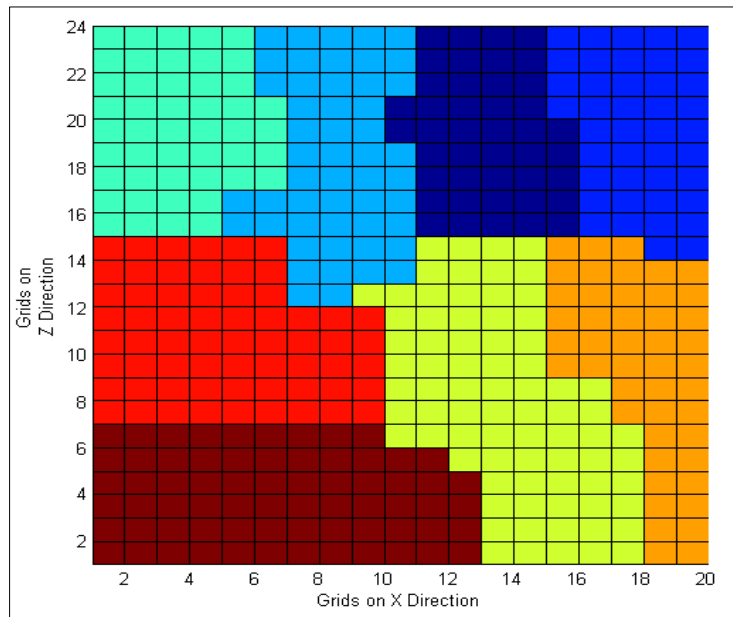


Figure 5-5 Partitioned graph of the 2-D compaction case. Different colors refer to the 8 different subdomains.

Table 5-1 shows the input parameters for two cases. Both cases are solved in two steps. In the first step, we apply the compaction force on the top of the material. We run this simulation for a sufficient long time to reach an equilibrium state for the material. In the second step, we remove the compressive stress and let the water inside the material drain from its two sides. We then plot the pore pressure of the center grid block versus time.

The difference of the results between any two cases with different number of processors is always less than 0.1%, so we only present the results with 8 processors, shown in Figure 5-6. As

the permeability of the material increases, the fluid drains more quickly and thus the peak of pore pressure comes earlier. From this comparison, we can draw the conclusion that a reservoir with higher permeability reacts faster than one with lower permeability.

Figure 5-6 also shows the comparison between THM-EGS’s results and the analytical solution. We find out that our numerical results match well with the analytical solution, verifying the accuracy of our simulator.

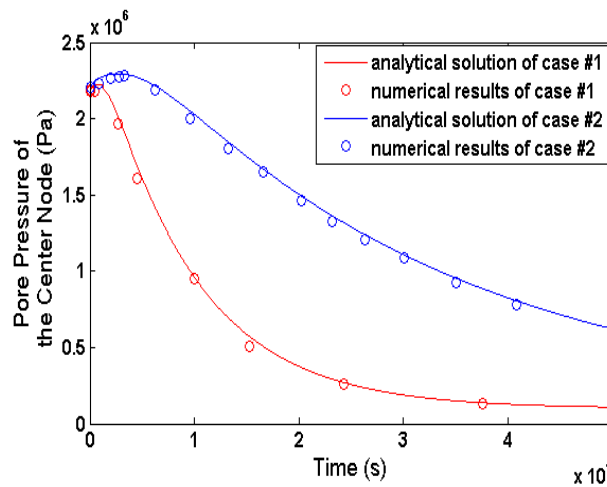


Figure 5-6 Comparison between numerical results and numerical results (8 processes) of 2-dimensional compaction. Red line refers to higher permeability case, while blue line refers to lower permeability case.

5.4.2 Field-Scale Case with Over a Million of Grid Blocks

We present a large reservoir grid to show the numerical performance of our simulator. The reservoir is in a size of 5km*5km*2.5km, fully saturated with water phase. There is a producing well in the center, penetrating 1km in Z direction. Figure 5-7 shows the mesh for the simulation case. The mesh is distributed logarithmically in the X and Y directions starting from the center, which is the simulation area of interest. There are a total of $129*129*100 = 1,664,100$ grid blocks in this simulation. We set the initial pore pressure to be 5MPa with constant pressure-

stress boundary condition and run the simulation for one year to get to an equilibrium state, which is then used as the initial condition for the next step of this problem. We then run the simulation for 4 years. As THM-EGS has already been verified in Chapter 5.04.1, we only show the numerical performance of the simulator.

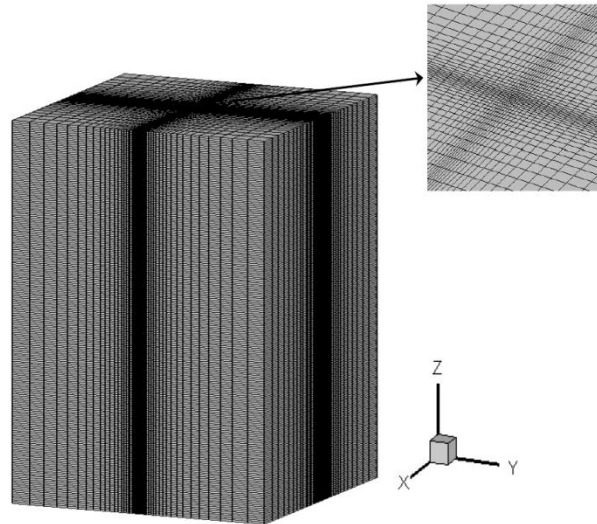


Figure 5-7 Problem description of the large reservoir case. The small picture on the top right is a close look of the area of interest.

The problem is run on a LINUX cluster with 32 computational nodes and 640 processors. Table 5-2 summarizes the numerical performance, including the number of processes, the total CPU time, and speedup factors. As THM-EGS cannot be run with single processor, the minimum number of processors we use is 2. As shown in Table 5-2 on page 46, the speedup at low number of processors is very close to linear. As such, we assume a linear speedup from the 2-processor case. We then multiply the CPU time of 2-processor case by 2 to estimate the CPU time of 1-processor serial case, as shown in the first row of Table 5-2. According to Table 5-2, the speedup of the case with 256 processors is 112.97.

Table 5-2 Summary of computation configuration and performance

No. of Processors	Total CPU Time (s)	Pre-processing Time (s)	Speedup	Ideal Speedup
1	188642.86			
2	94321.4	60.42	2	2
4	48871.19	64.14	3.86	4
8	25876.93	64.35	7.29	8
16	14067.32	64.23	13.41	16
32	7421.03	64.16	25.42	32
64	4701.96	67.53	40.12	64
128	2697.42	69.35	69.92	128
256	1669.85	73.42	112.97	256

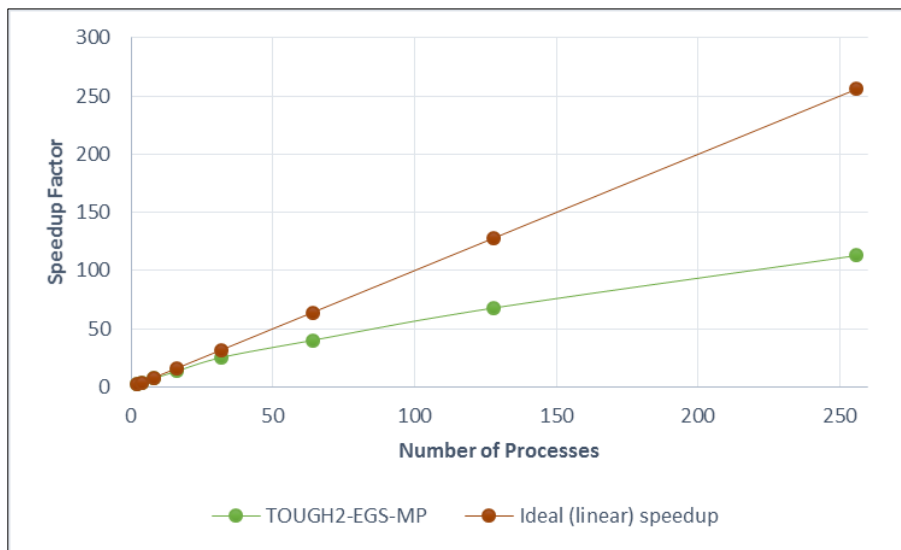


Figure 5-8 Comparison of the parallel speedup between THM-EGS and ideal performance.

Table 5-3 Summary of the number of inner (UPDATE) and border (EXTERNAL) elements per processor for each case

No. of Processors	Average No. of Inner Elements	Average No. of Border Elements	Inner-Border Ratio
16	104000	3190	32.6
32	52000	2023	25.7
64	26000	1333	19.5
128	13000	1008	12.9
256	6500	878	7.4

Figure 5-8 on page 46 gives the plot of speedup versus number of processors. According to Figure 5-8, the first several points indicate a linear speedup. Such trend is slowed as the number of process continues to increase. The reasons for this are as follows. On the one hand, as shown in Table 5-2, the time spent in the parallel preprocessing part is almost the same for cases with different number of processors. This is due to the lack of scalability of the master-slave framework used in this simulator. On the other hand, according to Table 5-3, as the whole reservoir is partitioned into more subdomains, more elements are exposed by the partition and become the elements on the borders. As such, the fraction of border (EXTERNAL) elements increases, resulting in more communication and more overlap of work between neighboring subdomains. Therefore, as number of processors increases, the more time is spent on preprocessing relatively and more communication is involved, so the speedup has to be slowed down to some extent.

In general, although several factors may limit the maximum speedup, the speedup is more than 100 times and the total CPU time has been decreased from more than one day (36 hrs) to

less than one hour (1669 s) for one to 256 processors. Therefore, THM-EGS can greatly speed up the numerical analysis of large reservoirs.

CHAPTER 6

NUMERICAL STUDY OF COLD WATER INJECTION

In this section, we will use THM-EGS and the proposed approach to study a real industrial case. The research will focus on an EGS project in Cooper Basin, Australia. This project is undertaken by Geodynamics Limited. They have drilled more than 10 wells in the area, within which several wells have been connected with each other by natural or engineered fractures, forming the hydraulic connected wells.

The geological map of the EGS field in interest is shown in Figure 6-1 on page 60. The conceptual model of three hydraulic connected wells in Cooper Basin is shown in Figure 6-2 on page 60. Chen and Wyborn (2009) have briefly studied this problem using discrete fracture approach with Excel. In their work, they assumed the fluid flow to be isothermal and ignored the mechanical effect. However, as illustrated above, thermal and mechanical processes are rather important in geothermal problems and cannot be simply ignored.

In this work, we will use more comprehensive numerical tool to study this problem, especially the THM behaviors of the fractures. We will study how the cold water injection alters the properties of the reservoir.

6.1 Homogeneous Case with Higher Permeability

A case has been run, in which one cold water injector and one hot water producer locate symmetrically in the two boundaries of an EGS reservoir. The EGS reservoir is simulated with the dual-porosity approach. The reservoir is 2500ft*2500ft*500ft. The initial pressure is 7.0MPa and the initial temperature is 220°C. Cold water of 80°C is injected for 7 years at the constant rate of 12kg/s from the injection well. The production well is producing at a constant bottom hole

pressure of 5.0MPa. As the mechanical properties are not given, they are looked up in the work of Fakcharoenphol (2012). The reservoir is 4km in depth.

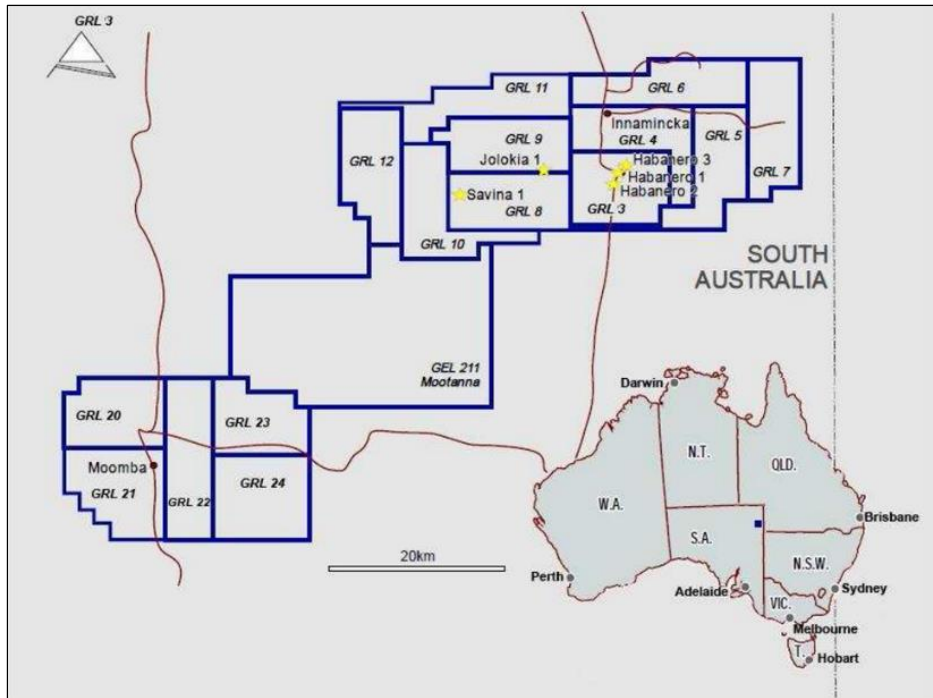


Figure 6-1 Site location map of the interested field in Cooper Basin, Australia (Chen and Wyborn, 2009).

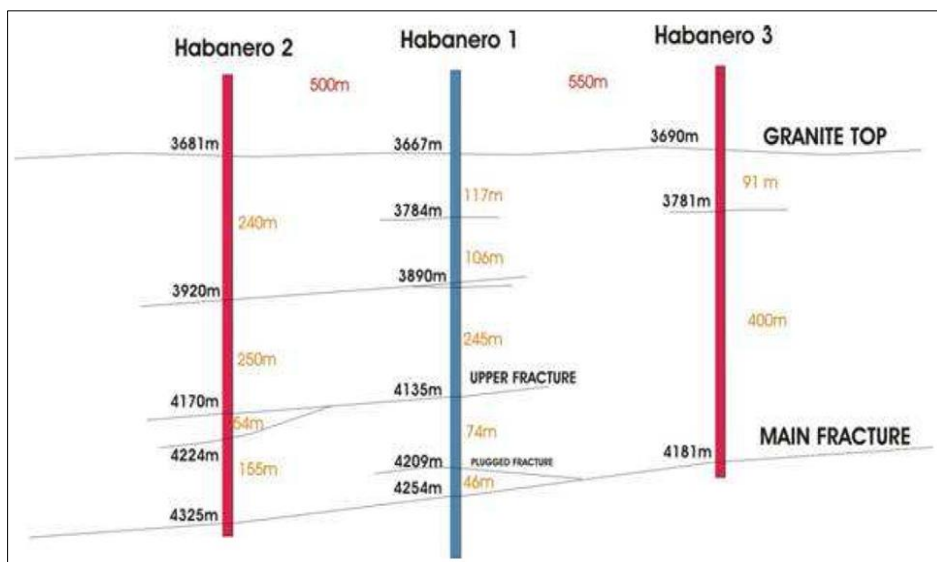


Figure 6-2 Three hydraulic connected wells in Cooper Basin.

The problem description is shown in Figure 6-3 and the input parameters are listed in Table 6-1. Basically, as shown in the problem description figure, there should be an impermeable caprock zone above the geothermal layer. The caprock zone is not directly simulated in this work. Actually, we assume the caprock to be all sandstone and use the density of it to estimate the gravity force of the caprock zone, which is 90MPa. We then assume the gravity to be the vertical stress and use the gravity to form the stress boundary condition in the vertical direction.

We assume the horizontal stress $v_{max,hor}$ and $v_{min,hor}$ to be

$$v_{max,hor} = v_{min,hor} = 0.7v_{ver} \tag{6.1}$$

Therefore, $v_{max,hor} = v_{min,hor} = 63\text{MPa}$.

The change of the permeability field is shown in Figure 6-4, from which we can see that the permeability has been enhanced by around 2 orders of magnitude. Such results are consistent with the observation from real reservoir production.

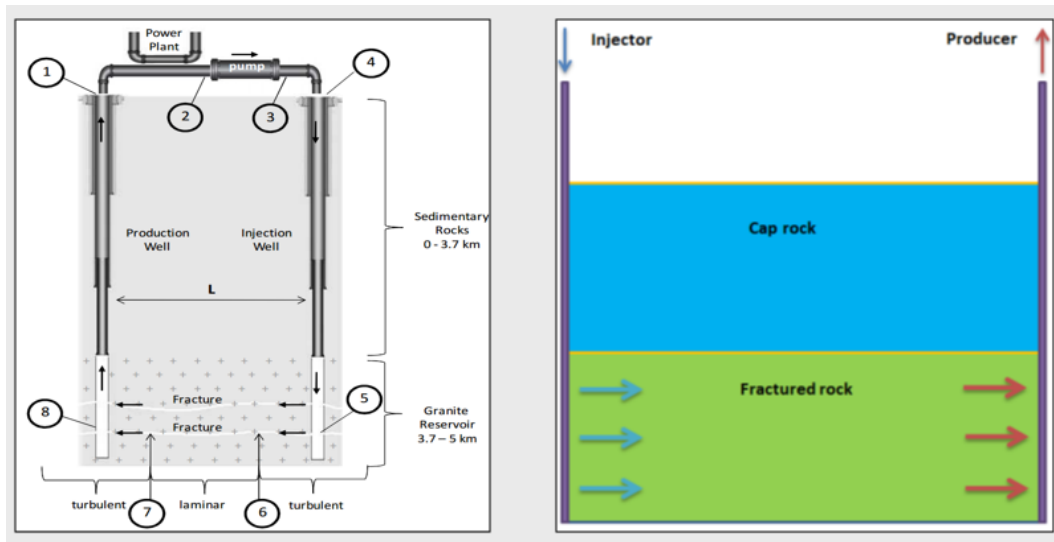


Figure 6-3 Left: conceptual model of water cycling system; right: problem setup in the simulator.

Table 6-1 Input parameters for high-permeability case

Properties	Values	Units
Initial permeability of the fracture	$K_{fx} = K_{fy} = 1.0 * 10^{-12}$ $K_{fz} = 1.0 * 10^{-13}$	m ²
Initial permeability of the matrix	$K_{mx} = K_{my} = 1.0 * 10^{-14}$ $K_{mz} = 1.0 * 10^{-14}$	m ²
Initial porosity of the matrix	0.02	dimensionless
Initial porosity of the fracture	0.001	dimensionless
Young's modulus	66.0	GPa
Fracture spacing	0.3	m
Poisson's ratio	0.25	dimensionless
Biot' s coefficient	1.0	dimensionless
Linear thermal expansion coefficient	7.9	10 ⁻⁶ m/(m K)
Thermal conductivity of dry rock	1.0	W/(m K)
Heat capacity of rock	1000	J/ (kg K)
Density of rock	2.5	10 ³ kg/m ³
ν_z	90	MPa
$\nu_{min,hor}/\nu_{max,hor}$	63	MPa

The initial aperture of fracture can be back calculated from the initial fracture permeability using the cubic law. In this case, the initial fracture aperture is 153 μm along the horizontal direction and 71 μm along the vertical direction.

The simulation is run on a cluster with 112 processes involved. The results are as follows. The permeability fields after 180 days and 7 years of injection are plotted in Figure 4. Because the permeability is relatively high in this case, the flow is fast in the channel between the two wells. Therefore, the permeability enhancement has a front, demonstrating the major flow

direction. The fracture pressure and temperature of injector is plotted in Figure 6-5, and the fracture aperture and the fracture permeability is plotted in Figure 6-6.

As demonstrated by the results, while the fracture aperture is enhanced by 100%, the fracture permeability is enhanced much more greatly (900%) near the cold water injector. This is because of the cubic law, that the fracture permeability is very sensitive to fracture aperture.

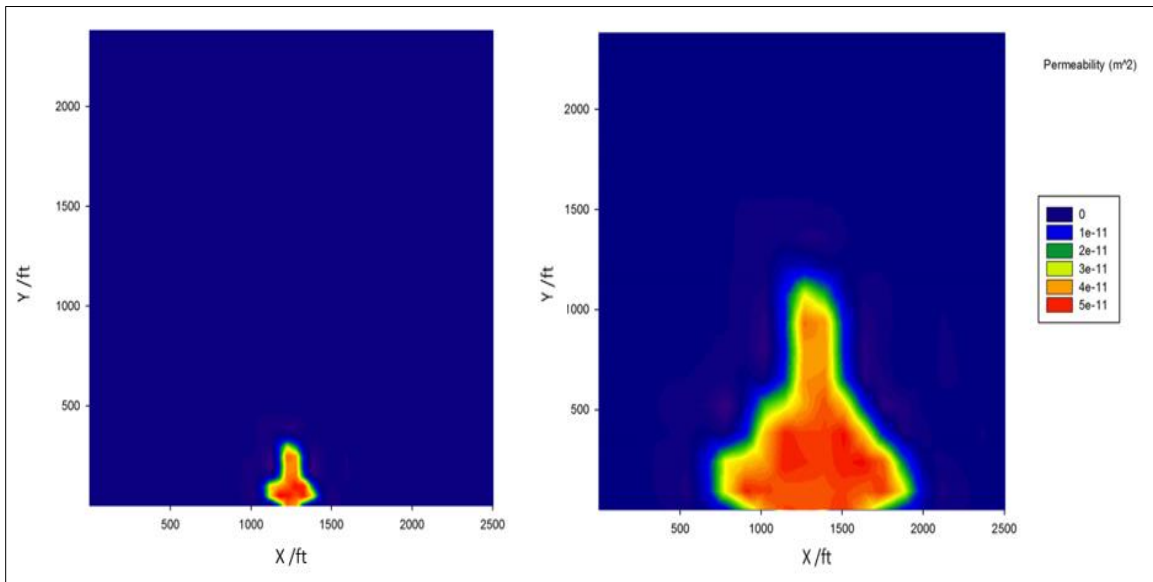


Figure 6-4 Permeability change after cold water injection. Red/orange color indicates the permeability enhanced zone near the injector. The figure on the left is the y-permeability field at 180 days of injection, while the figure on the right is the y-permeability field at 7 years of injection. In this case $K_{f0}=10^{-11}m^2(\sim 10 \text{ Darcy})$.

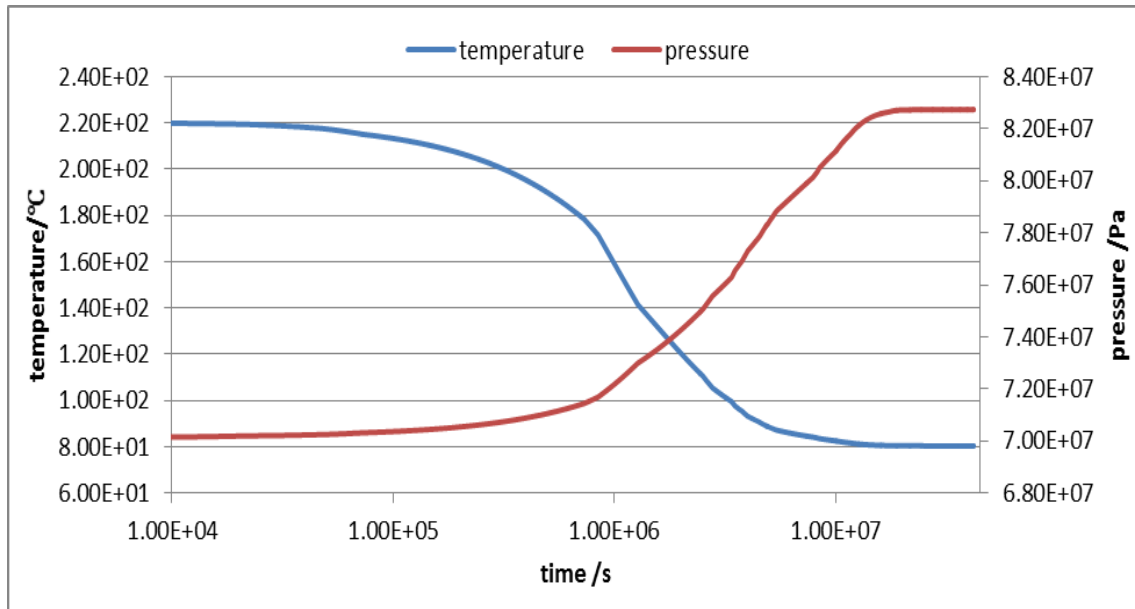


Figure 6-5 Pressure and temperature curve at cold water injector.

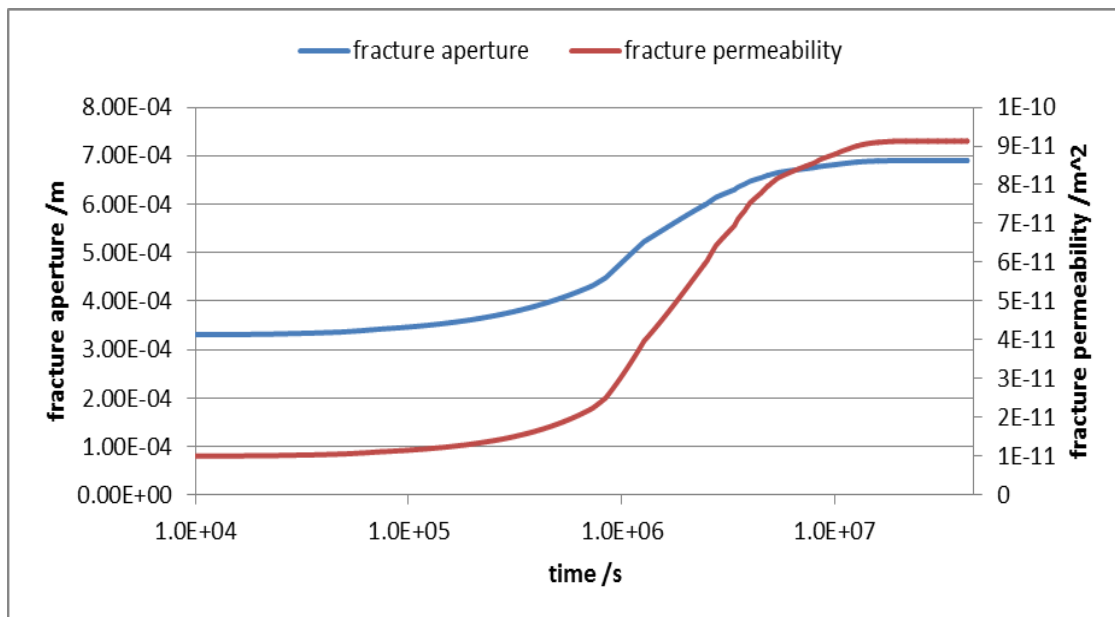


Figure 6-6 Fracture aperture and fracture permeability at cold water injector.

6.2 Homogeneous Case with Lower Permeability

In this case, we set the fracture permeability as approximately 1 Darcy (10^{-12} m^2). The other parameters are kept as the same to those of the first case. The permeability field is shown

in Figure 6-7. As demonstrated by the results, there is not a clear front of the permeability enhancement. This is because that the fracture permeability in this case is relatively lower compared to that in the first case. The fluid flow along the major flux direction is not significantly faster than the fluid flow along other directions. The fracture aperture and fracture permeability are plotted in Figure 6-8. As demonstrated by the figure, the fracture aperture is enhanced by approximately 300% and the fracture permeability is enhanced by approximately 3500%. This means that the fracture permeability can be enhanced by 2 orders of magnitude.

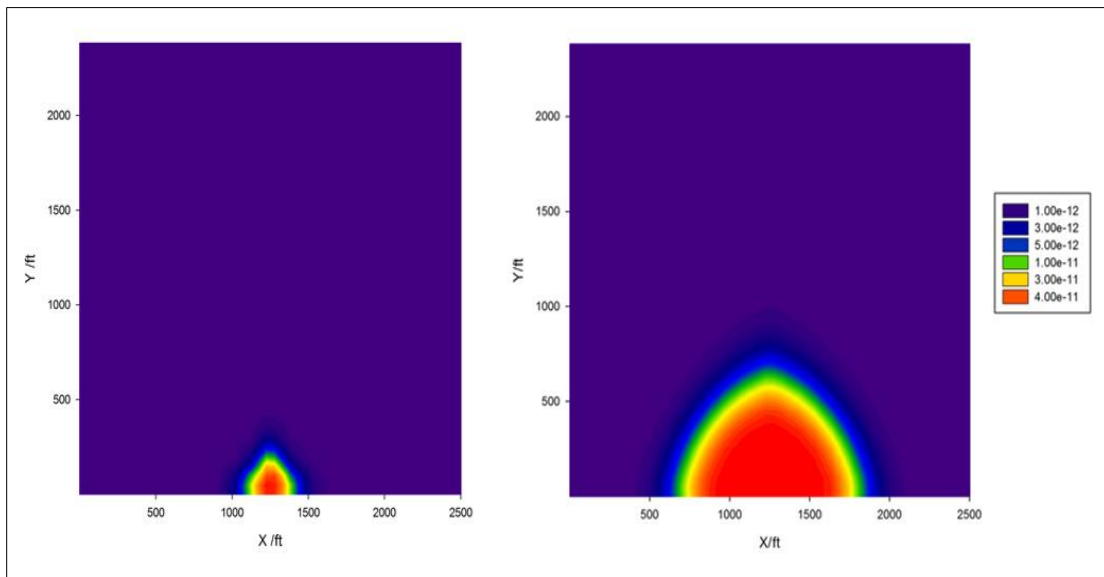


Figure 6-7 Permeability change after cold water injection. Red/orange color indicates the permeability enhanced zone near the injector. The figure on the left is the y-permeability field at 180 days of injection, while the figure on the right is the y-permeability field at 7 years of injection. In this case $K_{f0}=10^{-12}\text{m}^2(\sim 1 \text{ Darcy})$.

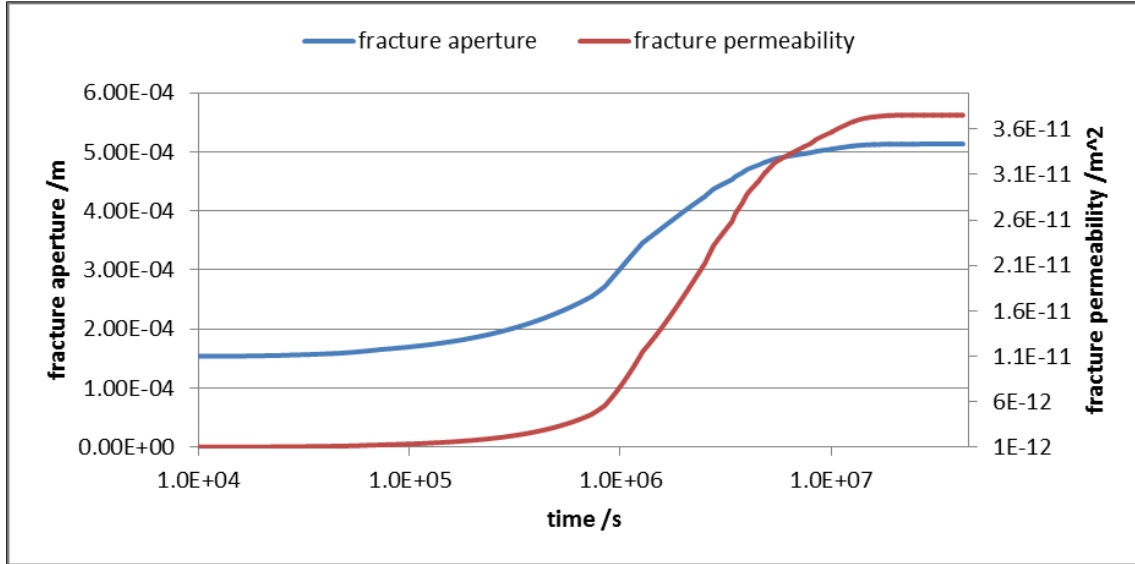


Figure 6-8 Fracture aperture and fracture permeability curve at cold water injector.

6.3 Sensitivity Analysis of Injection Temperature and Injection Rate

If we decrease the injection temperature from 80°C to 70°C, the fracture aperture will increase with 30 μm and the eventual fracture permeability will increase significantly from $3.75 \times 10^{-11} \text{m}^2$ (38.0 Darcy) to $4.51 \times 10^{-11} \text{m}^2$ (45.7 Darcy). And if we increase the injection temperature from 80°C to 90°C, the fracture aperture will decrease with 25 μm and the eventual fracture permeability will decrease from $3.75 \times 10^{-11} \text{m}^2$ to $3.21 \times 10^{-11} \text{m}^2$. The matrix permeability at the cold water injector is shown in Figure 6-11 on page 58. Compared to the fracture permeability, it is obvious that the matrix is much less sensitive to temperature change. As such, the fracture is the key to understand the behavior of fractured geothermal reservoir.

If we increase or decrease the fracture stiffness by 1 time and keep the other parameters fixed, the fracture permeability will have a change less than 20%, which means that the fracture permeability is not very sensitive to the stiffness of the fractures. This is because in this case the

matrix rock has a very large Young's modulus and the fracture spacing is relatively small. The sensitivity analysis of the fracture stiffness is shown in Figure 6-12 on page 58.

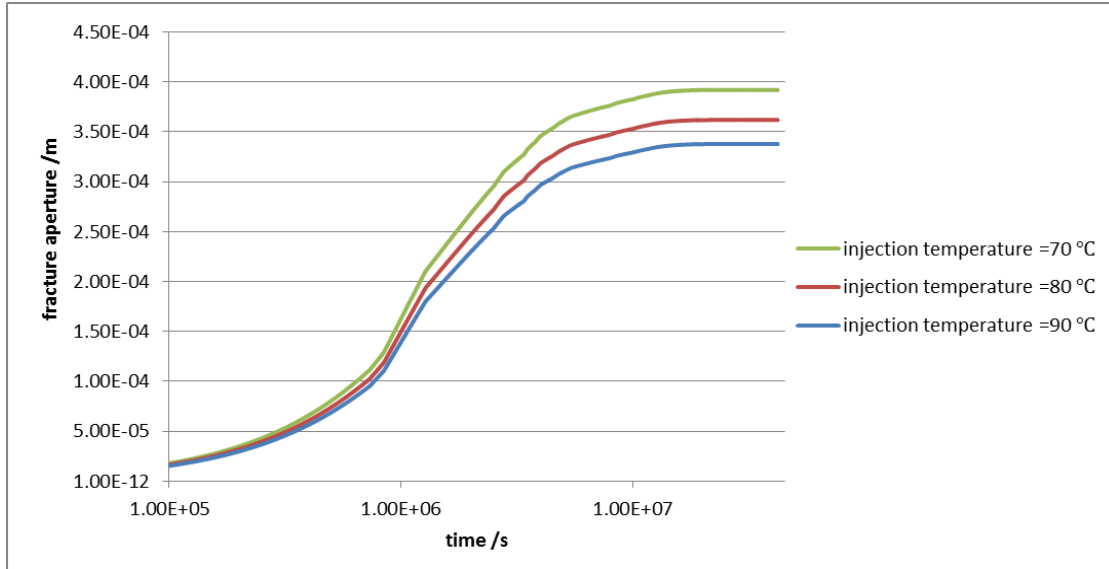


Figure 6-9 Fracture aperture at cold water injector with different injection temperature and fixed injection rate.

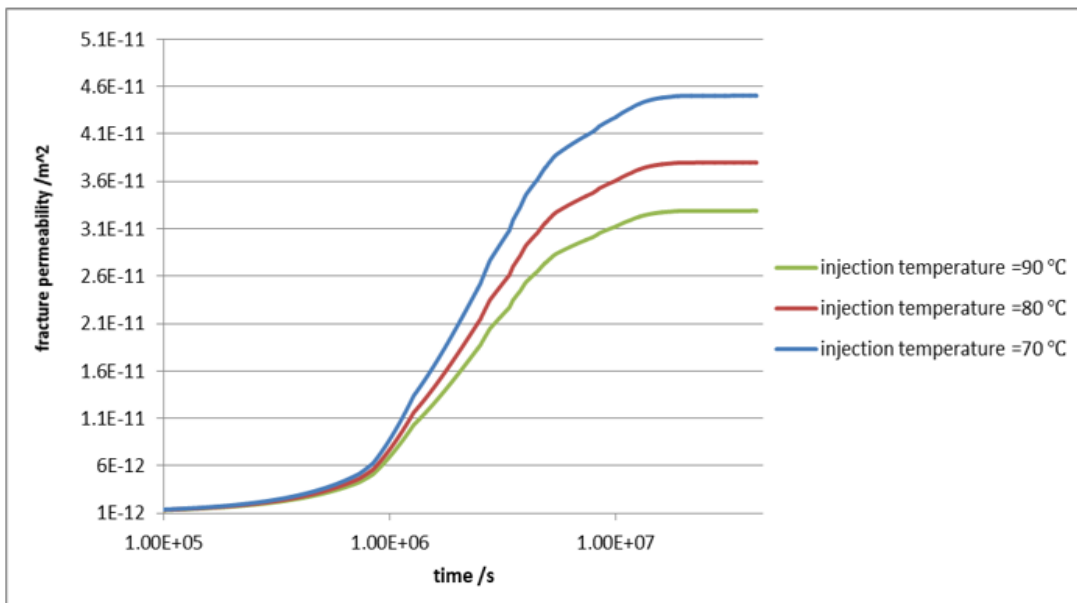


Figure 6-10 Fracture permeability at cold water injector with different injection temperature and fixed injection rate.

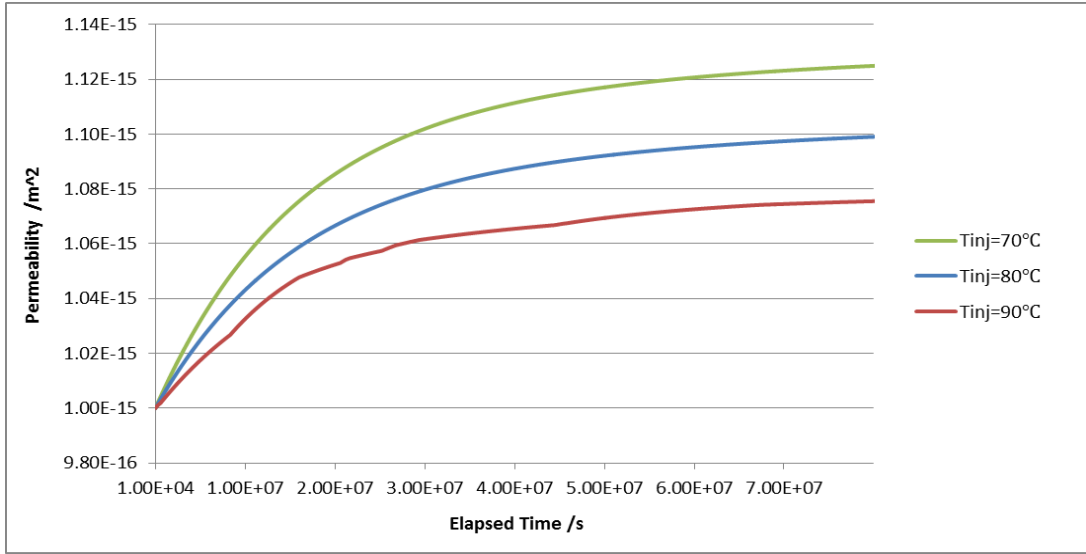


Figure 6-11 Matrix permeability at the cold water injector with respect to different injection temperature.

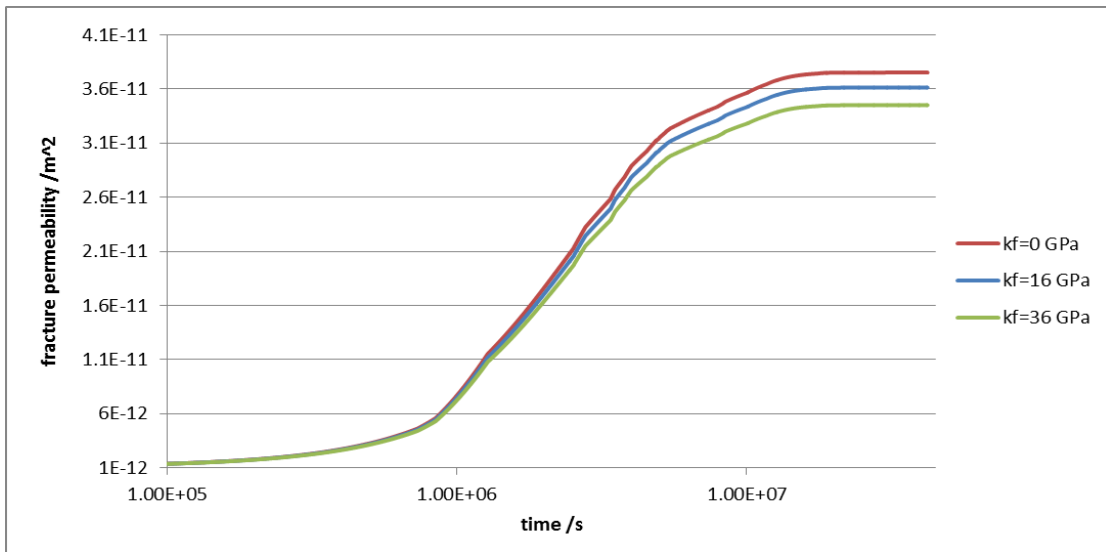


Figure 6-12 Sensitivity of fracture stiffness.

The fracture aperture and fracture permeability with respect to different injection rates is shown in Figure 6-13 and Figure 6-14 respectively. As demonstrated by the figures, the fractures are not very sensitive to change of injection rate. This is because the matrix rock in EGS is typically very stiff, so the compaction caused by pore pressure increase is not as significant as

the rock shrink induced by cold water injection. Therefore, compared to pressure, the temperature plays a more important role in the operation of EGS reservoirs.

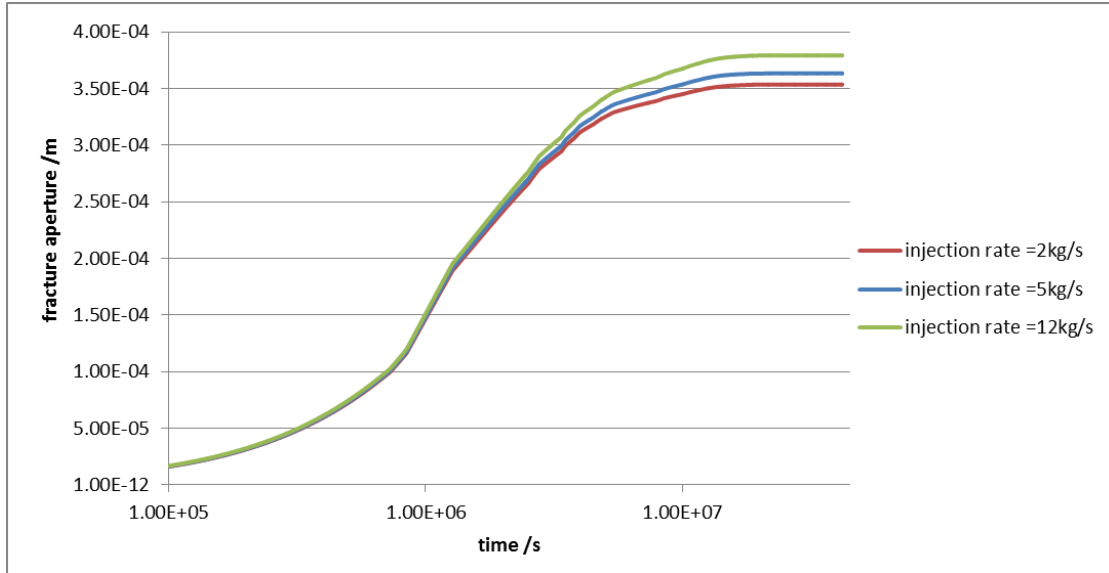


Figure 6-13 Fracture aperture at cold water injector with different injection rate and fixed injection temperature.

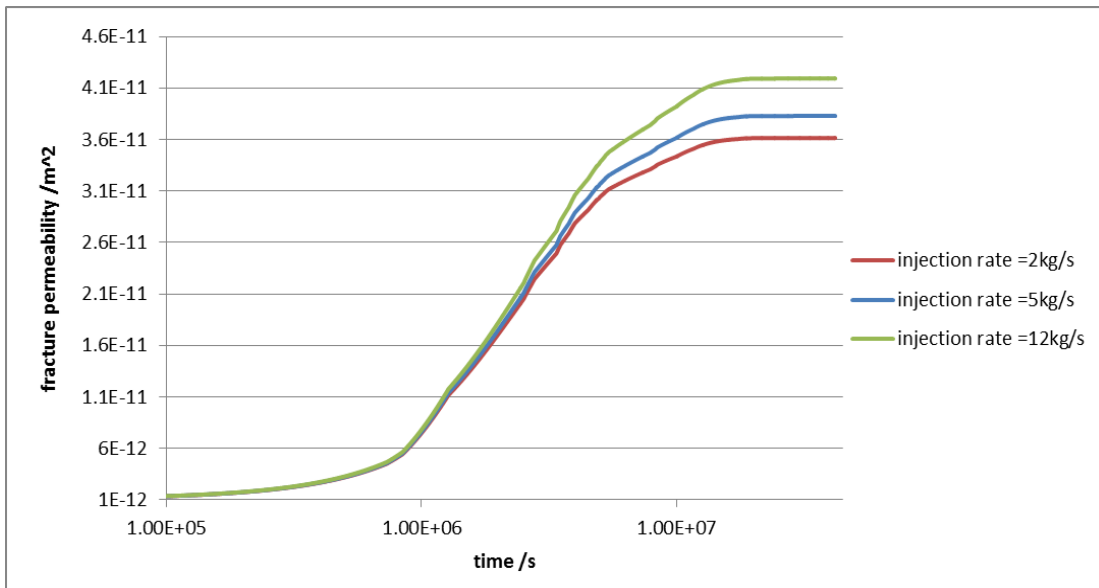


Figure 6-14 Fracture permeability at cold water injector with different injection rate and fixed injection temperature.

6.4 Extremely Low Permeable HDR with Fractured Zone

In this case, we assume that the hydraulic fracturing has created a fractured zone inside the HDR. The injector and producer are both drilled inside this fractured zone, so that the flow will mainly inside the fractured zone, as shown in the left of Figure 6-15. We set the width of the fractured zone to be 15m and the fracture permeability of it to be 1 Darcy (10^{-12}m^2). The permeability of the HDR zone is set to be (10^{-17}m^2), much lower than the fractured zone. The permeability field is shown in the right of Figure 6-15. The other parameters are the same as those used in Case 1, Cold water of 80°C is injected for 7 years with injection rate 15.5 kg/s.

As the results turn out, the thermal front reached the production well at 6.74 years (1214 days) after the start of injection. The permeability field at 180 days and 7 years after the start of injection is shown in Figure 6-16. As we can see, the permeability mainly changed inside the fractured zone. This is because that in this case the permeability of HDR is extremely low and liquid can hardly penetrated into the matrix. Therefore most flux exists inside the fracture zone, causing the fluid flow in fracture as well as the thermal front propagates much faster. The fracture permeability at the cold water injector is shown in Figure 6-17. We can see that the fracture permeability increases to the maximum value in much shorter time. This case shows the importance of fracture characterization, that different models of fracture network will lead to entirely different prediction of thermal front breakthrough.

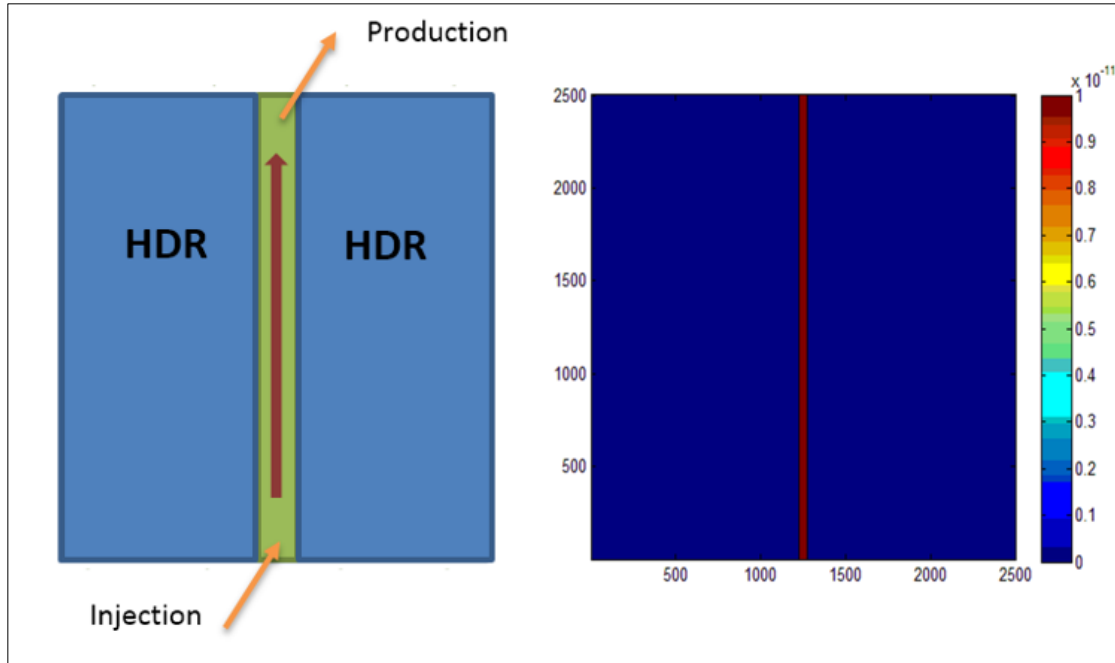


Figure 6-15 Left: conceptual model of fast flow channel in high-permeability zone; right: permeability field of this case.

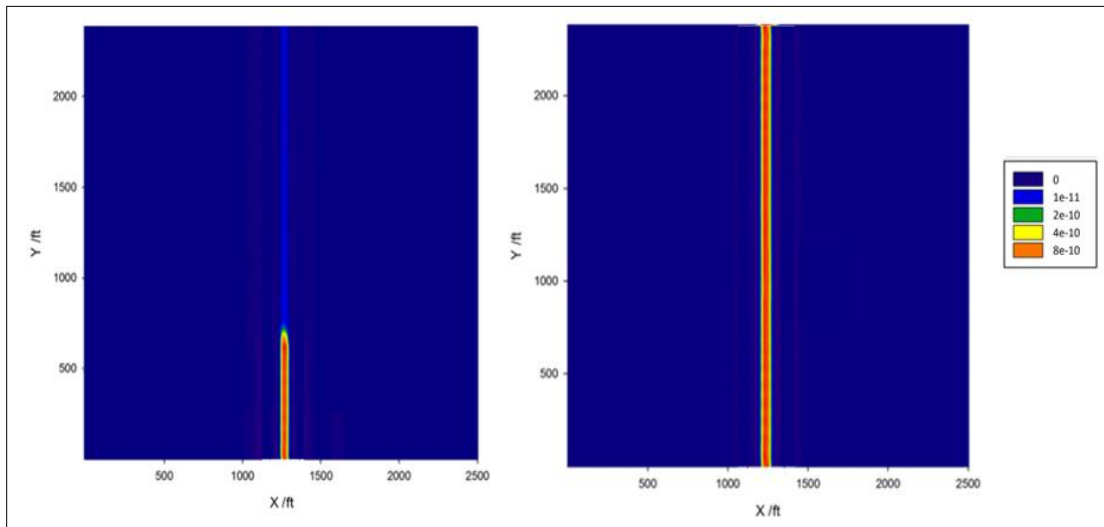


Figure 6-16 Permeability change after cold water injection. Red/orange color indicates the permeability enhanced zone near the injector. The figure on the left is the y-permeability field at 180 days of injection, while the figure on the right is the y-permeability field at 7 years of injection. In this case $K_{f0}=10^{-12}\text{m}^2(\sim 1 \text{ Darcy})$.

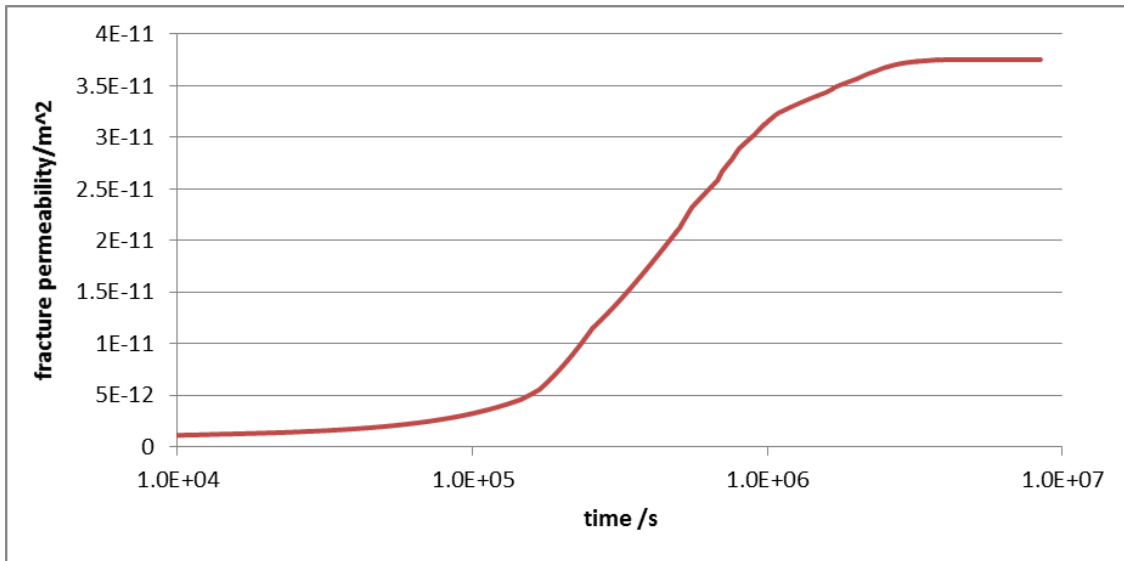


Figure 6-17 Fracture permeability at the cold water injector inside the fractured zone.

CHAPTER 7

MULTISTAGE PRECONDITIONING FOR THM PROBLEMS

7.1 Frequency of THM Coupled Problem

In this chapter, we will test the multi-stage preconditioning technique to improve the numerical performance of the linear solve in THM-EGS. Our effort will focus on adapting the traditional Constraint Pressure Residual (CPR) method (Wallis et al., 1985) to THM coupled problems. It has been proved that the pressure equation is close to elliptic partial equation and has global influence. Also, the saturation equation is of parabolic feature. The stress equation has no accumulation term at all, therefore it is of elliptic characteristic and of global influence.

Actually as the presumption of stress governing equation is that the system gets to equilibrium state within infinitely small time, the stress/strain change at one certain point will propagate to the whole reservoir in no time.

The temperature equation should be examined carefully. We plot the temperature field and the pressure field of the cold water injection problem in Figure 7-1 on page 64.

It is clear that, after 440 days of injection, the pressure change has already propagates to the entire reservoir, while the temperature change only occurs around the cold water injector. The difference between the two fields indicates the difference between the two equations. Since the temperature change propagates slowly and has only local influence, the temperature is similar to the saturation equation and shall be solved in the second stage of the multi-stage preconditioning. Therefore, in our multi-stage preconditioner, we will constrain the pressure and stress equations in the first stage, and solve the full system in the second stage. The details of the algorithm are as follows.

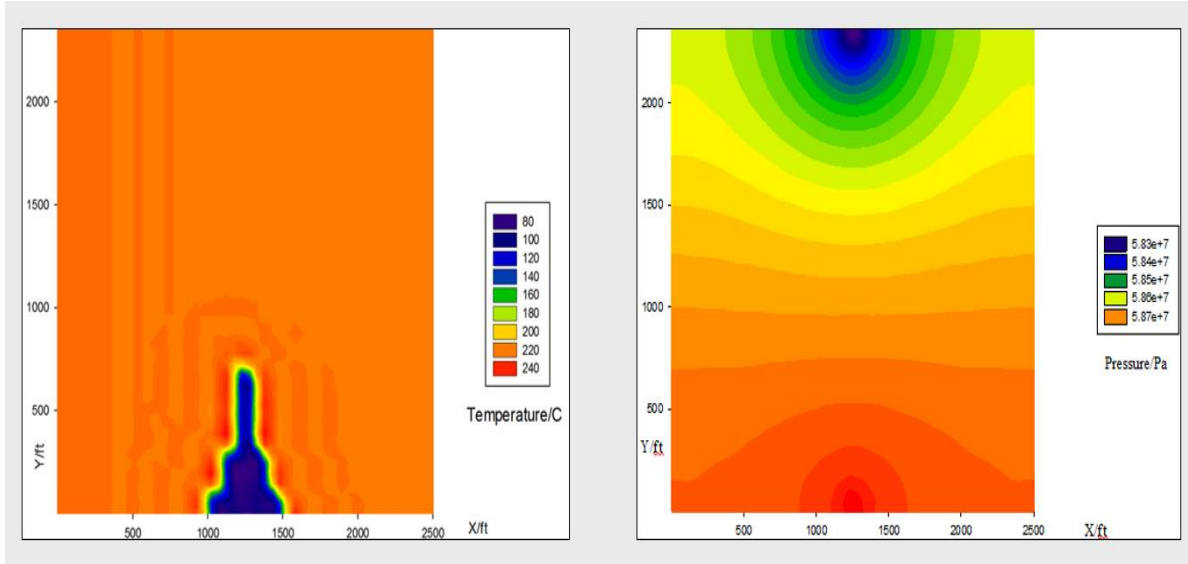


Figure 7-1 Comparison between temperature field and pressure field after 440 days of cold water injection.

7.2 Description of Algorithm

Consider the linear equation system

$$Au = f \quad (7.1)$$

Where the structure of the i th sub-block in the unknown array u is as follows

$$u_i = u_i \begin{bmatrix} \text{pressure} \\ \text{saturation} \\ \text{temperature} \\ \text{stress} \end{bmatrix} \quad (7.2)$$

The above sub-block is the typical primary variable (unknown) block of a THM coupling problem. Here the first equation is assumed to be the pressure equation while the last equation is assumed to be the stress equation. We solve the pressure equation and the stress equation to an approximate solution in the first stage to eliminate the low frequency components.

We aim to precondition the linear system as

$$P^{-1}Au = P^{-1}f \quad (7.3)$$

where P is the preconditioner.

Within each stage of the preconditioning processes, the unknowns are undated, so for a n -stage preconditioner, the unknowns are solved as follows

$$u^n - u^0 = \sum_{i=1}^n \delta u^i \quad (7.4)$$

where

$$\delta u^i = P_i^{-1} r^{i-1} \quad (7.5)$$

P_i is the preconditioner in the i th stag and r^{i-1} is the residual at the $i-1$ th stage. In the first stage, r^0 is calculated from the primary variables at the previous iteration step as

$$r^0 = f - Au^0 \quad (7.6)$$

Then for each stage, the residual is updated as

$$r^{i-1} = (I - AP_i^{-1}) r^{i-1} \quad (7.7)$$

Then a two stage preconditioner can be expressed as

$$P_M^{-1} = P_2^{-1} (I - AP_1^{-1}) + P_1^{-1} \quad (7.8)$$

Then we define a restrictor R as

$$R = \begin{bmatrix} e_p & 0 & 0 \\ \vdots & \ddots & \vdots \\ 0 & 0 & e_p \end{bmatrix} \quad (7.9)$$

where

$$e_p = \begin{bmatrix} 1 & 0 \\ 0 & 0 \\ 0 & 0 \\ 0 & 1 \end{bmatrix} \quad (7.10)$$

e_p is constructed to restrict from each sub-block in A to the pressure and stress equations only.

Then a restricted matrix is introduced as

$$W^T = R^T \cdot \text{diag}^{-1}(A) \quad (7.11)$$

where $\text{diag}(A)$ is the diagonal blocks of matrix A . Here W^T consists the according pressure-stress components.

Then the multistage preconditioner is constructed as

$$P_M^{-1} \cdot r = P^{-1} [r - A \cdot (R \cdot (W^T A R)^{-1} \cdot (W^T r))] + R [(W^T A R)^{-1} \cdot (W^T r)] \quad (7.12)$$

In the above formulation, the term $(R \cdot (W^T A R)^{-1} \cdot (W^T r))$ is the first stage preconditioner. In this work, this first stage preconditioner does not solve the pressure-stress system exactly, instead it solves the system approximately to a relative residual in the order of 10^{-4} using GMRES (restart). P is the second stage preconditioner, applied to the full system. In this work, P is chosen as ILU (0)-GMRES (restart) from the AZTEC package.

To sum up, the multi-staging approach can be summarized as the follows.

- Restrict the system into the pressure-stress subsystem.
- Solve the pressure-stress subsystem to an approximate solution x_{p-s} .
- Expand the solution x_{p-s} back to the fully system as Cr_{p-s} .
- Correct the full system as

$$r = r - A(Cr_{p-s}) \quad (7.13)$$

- Solve the full system using the corrected solution.

The above algorithm has been implemented in THM-EGS. An advantage of this approach is that it doesn't require much modification on the original code.

7.3 Homogeneous Case

In this sub-session, we apply the multistage preconditioner to the homogeneous problem presented in Chapter 6. In this case, the fracture permeability varies dramatically, which will

increase the nonlinearity of the problem, causing the linear solver to be unstable. The domain is discretized into $100 \times 50 \times 12 = 60,000$ grid blocks. We record the number of iterations for the linear solver to get converged within one Newton step. We also record the time spent in the linear solver within one time step.

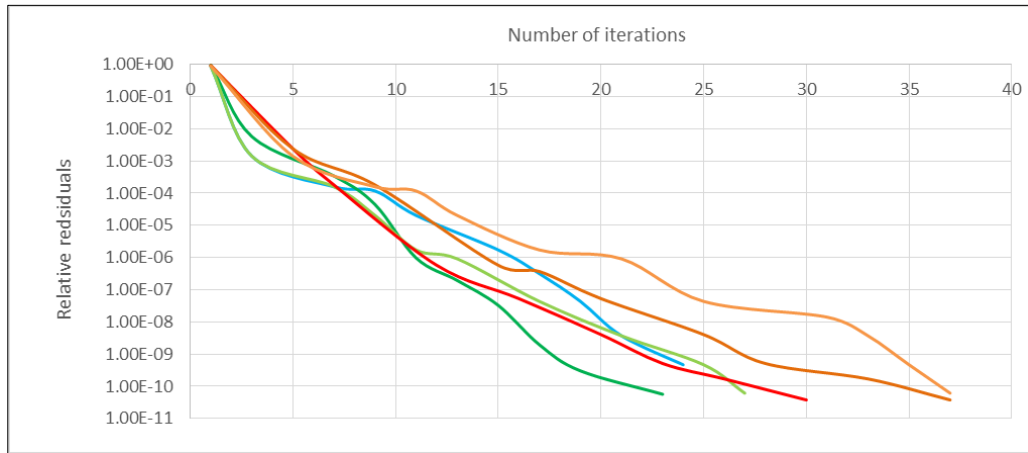


Figure 7-2 Performance of the multi-stage preconditioning for homogeneous permeability field. The blue/green lines demonstrate the numerical performance of linear solver with multi-stage preconditioning. The red/yellow lines demonstrate the numerical performance of linear solver without multi-stage preconditioning.

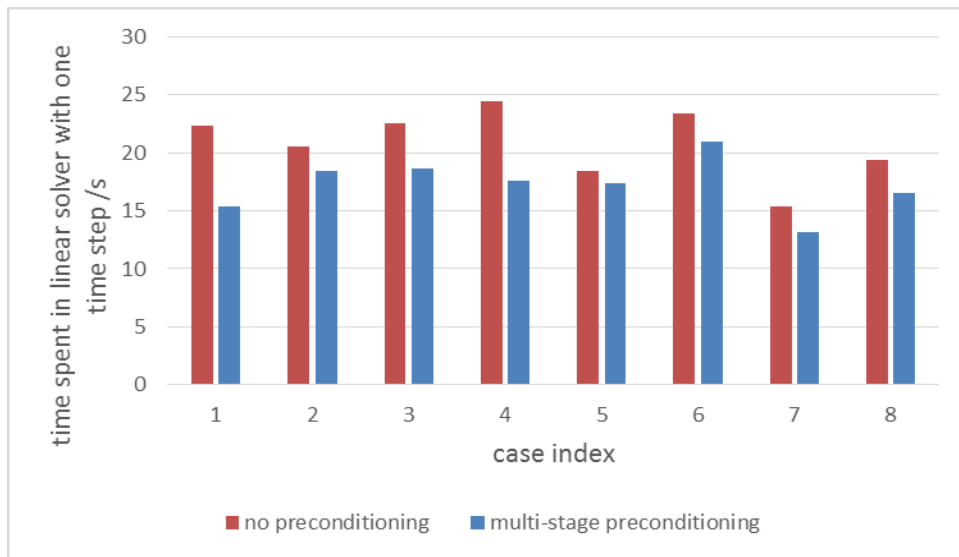


Figure 7-3 Comparison of the numerical performance between previous linear solve and multi-stage preconditioned linear solver in the homogeneous case.

As demonstrated by Figure 7-2 and Figure 7-3 on page 84, the number of iterations has been reduced by 25% by the multistage preconditioner (blue/green lines). As to the entire CPU time, the multistage preconditioner reduces the time spent in linear solver by 15% within each time step.

7.4 Homogeneous Case with Fractured Zone

In this sub-session, we apply the multistage preconditioner to the fractured zone presented in Chapter 6. This case is more challenging than the first case. In this case, besides the nonlinearity introduced by the permeability variation, the flow speed inside the fractured zone is much higher than the first case, affecting the numerical performance of the linear solver. The domain is discretized into $100 \times 50 \times 12 = 60,000$ grid blocks, shown in Figure 7-4. We record the number of iterations for the linear solver to get converged within one Newton step. We also record the time spent in the linear solver within one time step.

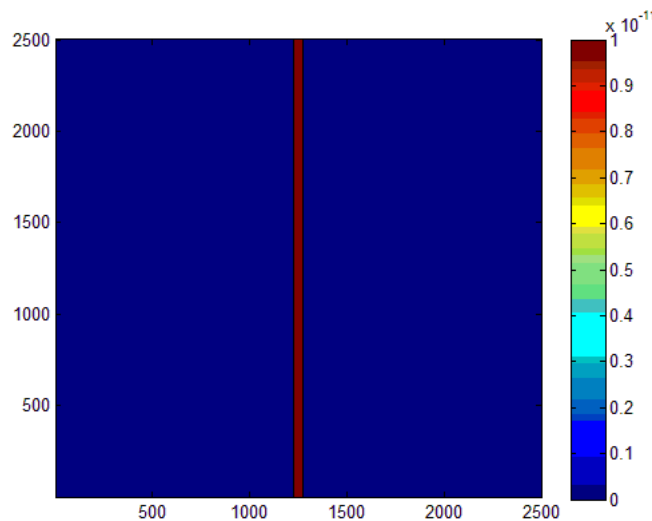


Figure 7-4 Homogenous permeability field with fractured zone. The permeability is in the unit of m^2 .

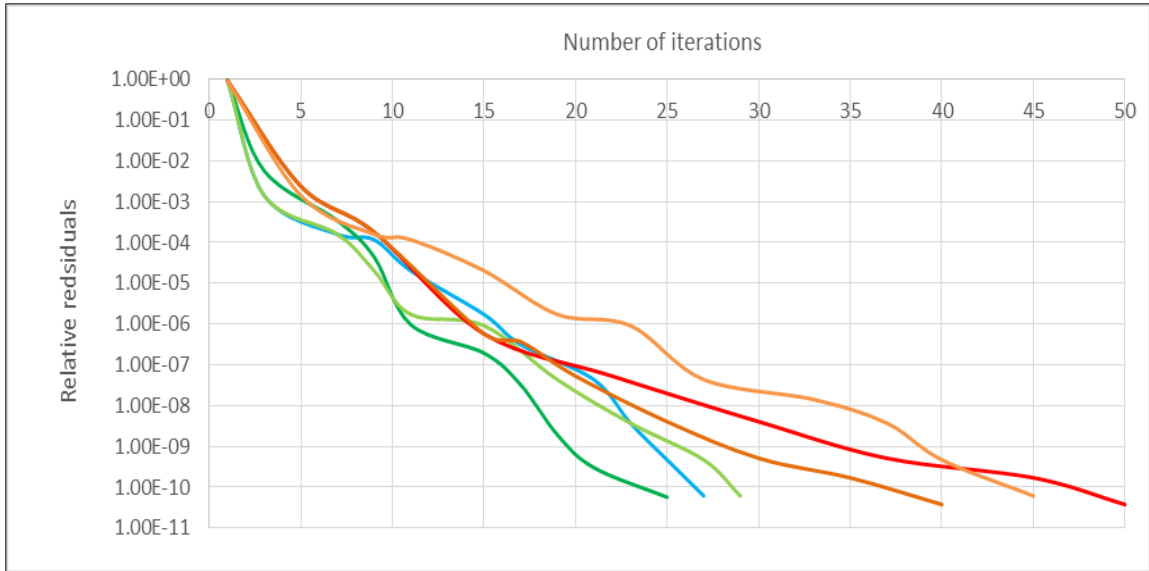


Figure 7-5 Performance of the multi-stage preconditioning for homogeneous permeability field with fractured zone. The blue/green lines demonstrate the numerical performance of linear solver with multi-stage preconditioning. The red/yellow lines demonstrate the numerical performance of linear solver without multi-stage preconditioning.

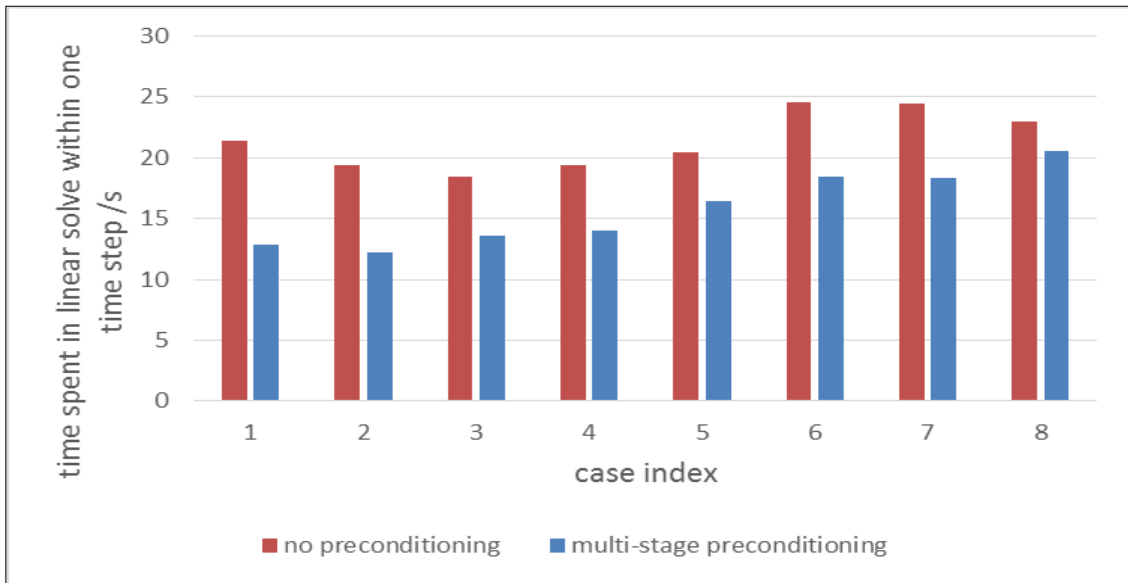


Figure 7-6 Comparison of the numerical performance between previous linear solve and multi-stage preconditioned linear solver in the homogeneous permeability field with fractured zone.

As demonstrated by Figure 7-5 on page 69, the number of iterations has been reduced by about 40% by the multistage preconditioner (blue/green lines). As to the entire CPU time, the multistage preconditioner reduces the time spent in linear solver by about 25% within each time step, shown in Figure 7-6 on page 69. We can see that compared to the first case, the multistage preconditioner performs better in this case. This is because that the first stage preconditioner can provide a good guess. For heterogeneous cases, the multistage preconditioner can greatly improve the numerical performance of the linear solver.

7.5 Highly Heterogeneous Case

In this sub-session, we test the multistage preconditioner to a highly heterogeneous case. We generate a heterogeneous permeability field subject to normal distribution, shown in Figure 7-7. The average permeability is set to be 1 Darcy. The standard derivation of the random field is set to 5. In the field, the highest value is 150 times of the lowest value. Obviously this case is very challenging to the linear solver. The domain is discretized into $100*50*12=60,000$ grid blocks. As demonstrated by Figure 7-8, if the linear solver is not with multistage precondition, the system becomes extremely difficult to get converged. In this case, the multistage preconditioner reduces the number of iterations by more than 60% and accelerates the simulation by about 50%, shown in Figure 7-9. This case indicates that the multistage preconditioner is very suitable to highly heterogamous problem. It turns out that the multistage preconditioning technique can significantly increase the stability of the linear solver, guaranteeing the success of reservoir simulation.

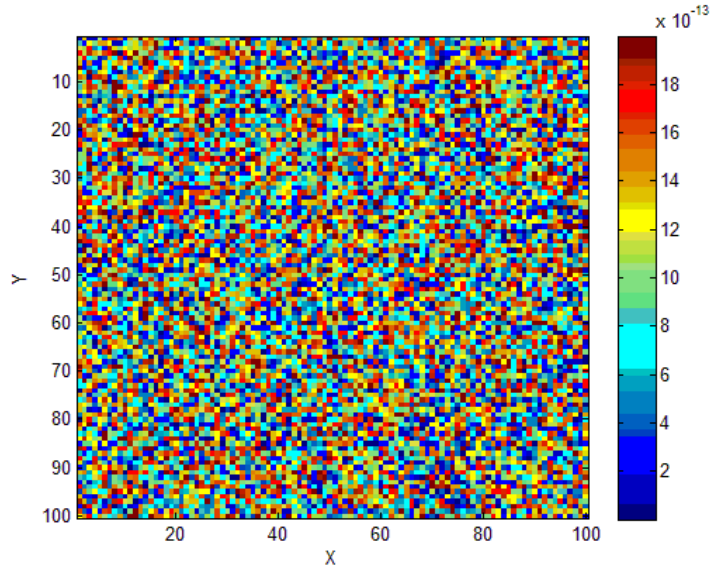


Figure 7-7 Heterogeneous permeability field. The permeability is in the unit of m^2 .

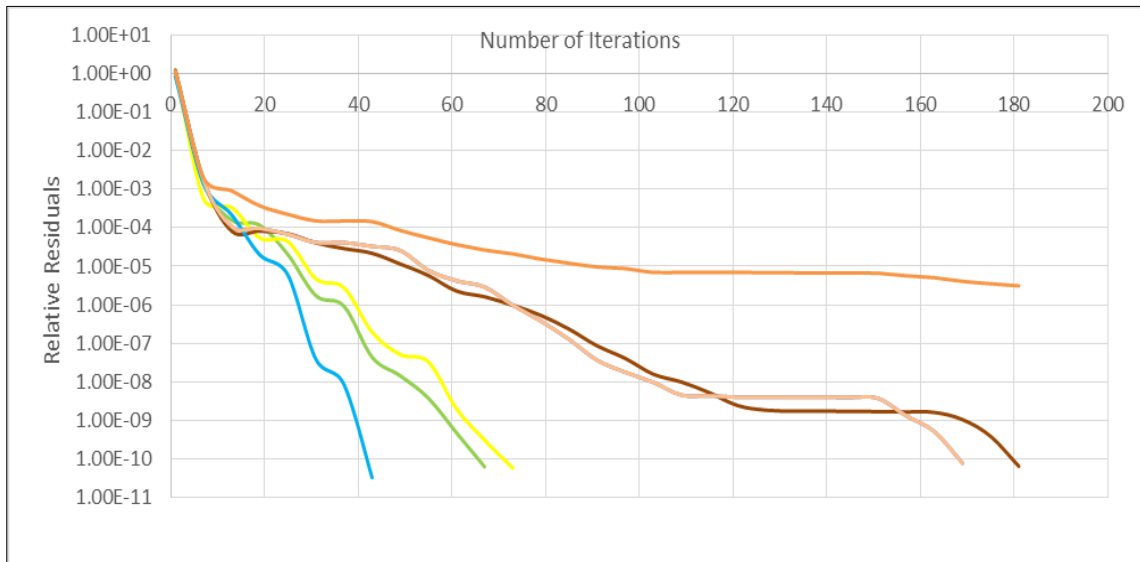


Figure 7-8 Performance of the multi-stage preconditioning for highly heterogeneous permeability field. The blue/green lines demonstrate the numerical performance of linear solver with multi-stage preconditioning. The red/orange lines demonstrate the numerical performance of linear solver without multi-stage preconditioning.

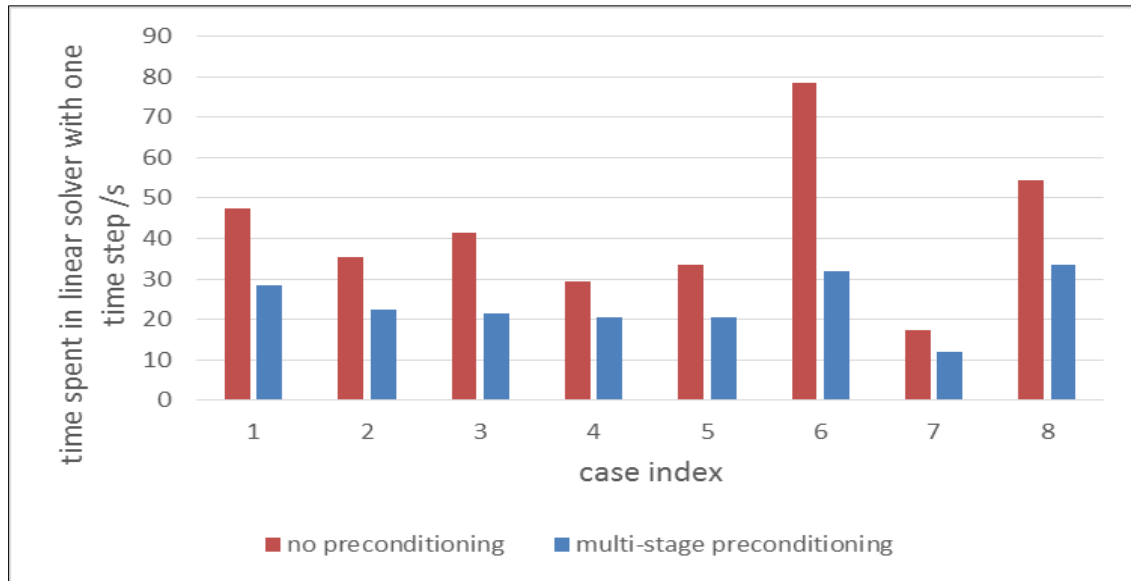


Figure 7-9 Comparison of the numerical performance between previous linear solve and multi-stage preconditioned linear solver in the homogeneous case.

CHAPTER 8

CONCLUSION AND DISCUSSION

In this chapter, we draw conclusions and point out the limitations of this work.

8.1 Summary and Conclusion

In this work to pursue Master of Science degree,

- A fully coupled THM massively parallel simulator, THM-EGS, has been developed. The simulator can precisely predict the combined thermal-hydraulic-mechanical behavior of geothermal reservoirs. The simulator is fully object oriented, making itself extensible to further modification. With its powerful parallel framework, the parallel simulator can accelerate computation by hundreds of times, much beyond most commercial simulators.
- The results of mean stress approach has been verified against the analytical solution of the Mandel-Cryer's problem. The mean stress approach has shown its accuracy and convenience in geomechanical simulation. It is able to simulate the stress-strain field with very limited newly added computational load.
- A semi-analytical correlation of thermal induced fracture aperture change is derived. The correlation can capture and quantify the influence of temperature and pressure change on the fracture aperture. Therefore, with this correlation, the permeability enhancement effect near cold water injectors can be captured and studied. It turns out that the permeability can be enhanced by 2 orders of magnitude by cold water injection into a hot geothermal reservoir. In an EGS reservoir where matrix rock is very stiff, the temperature of the injection fluid plays a more important role than the injection rate. The characterization of fracture network is also very important for the prediction of the fracture behaviors.

- A multistage preconditioner has been implemented in THM-EGS simulator and has significantly improved the speed of the linear solver, especially when the permeability field is highly heterogeneous.

8.2 Suggestions for future work

- The limitation of the fracture aperture change correlation is that the fracture in this correlation is assumed to be two infinitely long parallel plates. However, the real fracture has finite length, as shown in the following figure. Such difference may result in overestimation of the fracture aperture increase predicted by the proposed correlation.

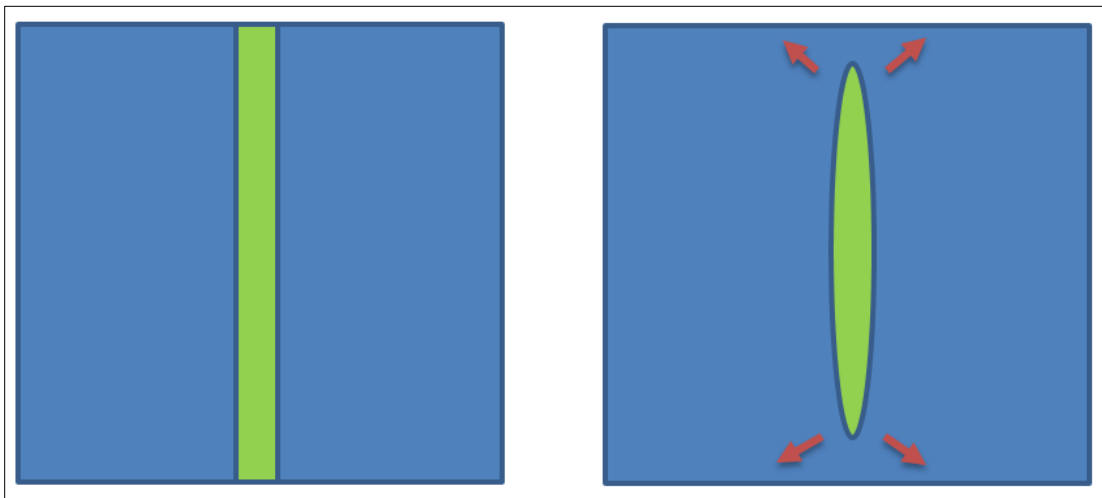


Figure 8-1 Comparison between fracture model used in THM-EGS correlation and in real reservoirs.

- As discovered by Hakami and Larsson (1996), the real fracture plane is not smooth and the fracture aperture is not a constant, but a probabilistic function. Given this fact, the aperture change should also be estimated by probabilistic approach. The related research remains a hot topic.

- The mean stress approach has the limitation that it cannot capture all the components of the stress tensor. In the future, a more advanced approach that can solve the entire stress tensor should be developed.
- In this work, we mainly test the multi-scale preconditioning technique with homogeneous and heterogeneous problems. In order to apply this technique into real applications, more complex problems, including compositional modeling with phase changes and reservoirs with larger faults, should be tested.

REFERENCES CITED

- Abousleiman, Y., Cheng, A.D., Cui, L., Detournay, E. and Roegiers, J.C. 1996. Mandel's problem revisited. *Geotechnique* **46**(2): 187-195.
- Alm, P. 1999. Hydro-mechanical behavior of a pressurized single fracture: an in situ experiment. PhD Thesis, Chalmers University of Technology, Gothenburg, Sweden
- Bai, M. and Roegiers, J.C. 1994. Fluid flow and heat flow in deformable fractured porous media. *International Journal of Engineering Science* **32**(10): 1615-1633.
- Baghbanan, A. and Jing, L. 2007. Hydraulic properties of fractured rock masses with correlated fracture length and aperture. *International Journal of Rock Mechanics and Mining Sciences* **44**(5): 704-719.
- Bandis, S. C., Lumsden, A. C., and Barton, N. R. 1983. Fundamentals of rock joint deformation. *International Journal of Rock Mechanics and Mining Sciences & Geomechanics Abstracts* **20**(6): 249-268. Pergamon.
- Bandis, S. C. 1990. Mechanical properties of rock joints. *Proc., Rock Joints*. Balkema, Rotterdam, 2-7 June, 125-140.
- Barton, N., Bandis, S., and Bakhtar, K. 1985. Strength, deformation and conductivity coupling of rock joints. *International Journal of Rock Mechanics and Mining Sciences & Geomechanics Abstracts* **22**(3):121-140. Pergamon.
- Berkowitz, B. 1995. Analysis of fracture network connectivity using percolation theory. *Mathematical Geology* **27**(4): 467-483.
- Berkowitz, B. 2002. Characterizing flow and transport in fractured geological media: A review. *Advances in Water Resources* **25**(8): 861-884.
- Berryman, J. G., and Wang, H. F. 1995. The elastic coefficients of double - porosity models for fluid transport in jointed rock. *Journal of Geophysical Research: Solid Earth (1978–2012)* **100**(B12): 24611-24627.
- Bertani, R. 2007. World geothermal generation in 2007. *Proc., European Geothermal Congress*, Unterhaching, Germany, 30 May -1 June.
- Bertani, R. 2012. Geothermal power generation in the world 2005–2010 update report. *Geothermics* **41**(1): 1-29.
- Byerlee, J. 1978. Friction of rocks. *Pure and applied Geophysics* **116**(4-5): 615-626.

- Cao, H., Tchelepi, H. A., Wallis, J. R., and Yardumian, H. E. 2005. Parallel scalable unstructured CPR-type linear solver for reservoir simulation. Presented at the SPE Annual Technical Conference and Exhibition, Dallas, Texas, 9-12 October. SPE-96809-MS. <http://dx.doi.org/10.2118/96809-MS>.
- Cappa, F., Guglielmi, Y., F  art, P., Merrien-Soukatchoff, V., and Thoraval, A. 2005. Hydromechanical interactions in a fractured carbonate reservoir inferred from hydraulic and mechanical measurements. *International Journal of Rock Mechanics and Mining Sciences* **42**(2): 287-306.
- Celia, M. A., Bouloutas, E.T., and Zarba, R.T. 1990. A general mass - conservative numerical solution for the unsaturated flow equation. *Water resources research* **26**(7): 1483-1496.
- Chen, D. and Wyborn, D. 2009. Habanero field tests in the Cooper Basin, Australia: A proof-of-concept for EGS. *Geothermal Resources Council Transactions* **33**(1): 159-164.
- Cook, N. G. W. 1992. Natural joints in rock: mechanical, hydraulic and seismic behaviour and properties under normal stress. *International Journal of Rock Mechanics and Mining Sciences & Geomechanics Abstract*, **29**(3), 198-223. Pergamon.
- Davies, J. P. and Davies, D. K. 2001. Stress-dependent permeability: characterization and modeling. *SPE Journal* **6**(2): 224-235. SPE-71750-PA. <http://dx.doi.org/10.2118/71750-PA>.
- Elmi, D. and Axelsson, G. 2009. Application of a transient wellbore simulator to wells HE-06 and HE-20 in the Hellisheidi geothermal system, SW-Iceland. *Proc.*, 34th Workshop on Geothermal Reservoir Engineering, Stanford, CA, 9-11 February.
- Elsworth, D. and Bai, M. 1992. Flow-deformation response of dual-porosity media. *Journal of Geotechnical Engineering* **118**(1): 107-124.
- Eslami, M. R., Hetnarski, R. B., Ignaczak, J., Noda, N., Sumi, N., and Tanigawa, Y. 2013. *Theory of Elasticity and Thermal Stresses*, first edition. London: Springer.
- Evans, K. F., Cornet, F. H., Hashida, T., Hayashi, K., Ito, T., Matsuki, K., and Wallroth, T. 1999. Stress and rock mechanics issues of relevance to HDR/HWR engineered geothermal systems: review of developments during the past 15 years. *Geothermics* **28**(4): 455-474.
- Fakcharoenphol, P., Hu, L., and Wu, Y. S. 2012. Fully-implicit flow and geomechanics model: application for enhanced geothermal reservoir simulations. *Proc.*, 37th Workshop on Geothermal Reservoir Engineering, Stanford, CA, 30 January - 1 February.
- Fridleifsson, I. B., Bertani, R., Huenges, E., Lund, J. W., Ragnarsson, A., and Rybach, L. (2008, January). The possible role and contribution of geothermal energy to the mitigation of climate change. *Proc.*, IPCC Scoping Meeting on Renewable Energy Sources, Luebeck, Germany. **20**(25): 59-80.

- Ghassemi, A., Nygren, A., and Cheng, A. (2008). Effects of heat extraction on fracture aperture: A poro-thermoelastic analysis. *Geothermics* **37**(5): 525-539.
- Ghassemi, A. and Suresh Kumar, G. 2007. Changes in fracture aperture and fluid pressure due to thermal stress and silica dissolution/precipitation induced by heat extraction from subsurface rocks. *Geothermics* **36**(2): 115-140.
- Gelet, R., Loret, B., and Khalili, N. 2012. A thermos-hydro - mechanical coupled model in local thermal non - equilibrium for fractured HDR reservoir with double porosity. *Journal of Geophysical Research: Solid Earth (1978-2012)* **117**(B7).
- Gries, S., St üben, K., Brown, G. L., Chen, D., and Collinns, D. A. 2014. Preconditioning for efficiently applying Algebraic Multigrid in fully implicit reservoir simulations. *SPE Journal* **19**(4): 726-736. SPE-163608-PA. <http://dx.doi.org/10.2118/163608-PA>.
- Gropp, W. 2002. MPICH2: A new start for MPI implementations. *Proc., 9th European PVM/MPI Users' Group Meeting, Linz, Austria, 29 September – 2 October, 7-7*.
- Hakami, E. and Larsson, E. 1996. Aperture measurements and flow experiments on a single natural fracture. *International Journal of Rock Mechanics and Mining Sciences & Geomechanics Abstracts* **33**(4): 395-404. Pergamon.
- Jaeger, J. C., Cook, N. G., and Zimmerman, R. 2009. *Fundamentals of rock mechanics*, fourth edition. New York: John Wiley & Sons.
- Jing, L. and Stephansson, O. 2007. *Fundamentals of Discrete Element Methods for Rock Engineering: Theory and Applications*, first edition Amsterdam: Elsevier.
- Karypis, G. and V. Kumar. 1995. Metis-Unstructured Graph Partitioning and Sparse Matrix Ordering System, Version 2.0, <http://citeseer.ist.psu.edu/viewdoc/summary?doi=10.1.1.38.376> (accessed 22 April 2014).
- Kawai, T. 1978. New discrete models and their application to seismic response analysis of structures. *Nuclear Engineering and Design* **48**(1): 207-229.
- Lee, H. S. and Cho, T. F. 2002. Hydraulic characteristics of rough fractures in linear flow under normal and shear load. *Rock Mechanics and Rock Engineering* **35**(4): 299-318.
- Lemmon, E. W., McLinden, M. O., and Friend, D. G. 2005. NIST Chemistry Webbook, <http://webbook.nist.gov/chemistry/fluid/> (accessed 7 July 2014).
- Lim, K. T., and Aziz, K. 1995. Matrix-fracture transfer shape factors for dual-porosity simulators. *Journal of Petroleum Science and Engineering* **13**(3): 169-178.

- Longuemare, P., Mainguy, M., Lemonnier, P., Onaisi, A., Gérard, C., and Koutsabeloulis, N. 2002. Geomechanics in reservoir simulation: overview of coupling methods and field case study. *Oil & Gas Science and Technology* **57**(5): 471-483.
- Mandel, J. 1953. Consolidation Des Sols (Étude Mathématique). *Geotechnique* **3**(7): 287-299.
- McKee, C. R., A. C. Bumb, and R. A. Koenig. 1988. Stress-dependent permeability and porosity of coal and other geologic formations. *SPE Formation Evaluation* **3**(1): 81-91. SPE-12858-PA. <http://dx.doi.org/10.2118/12858-PA>.
- McTigue, D. F. 1986. Thermoelastic response of fluid-saturated porous rock. *Journal of Geophysical Research: Solid Earth (1978–2012)* **91**(B9): 9533-9542.
- Message Passing Forum. 1994. A Message-Passing Interface Standard. *International Journal of Supercomputing Applications and High performance Computing* **8**(3-4).
- Narasimhan, T. N. and Witherspoon, P. A. 1976. An integrated finite difference method for analyzing fluid flow in porous media. *Water Resources Research* **12**(1): 57-64.
- Norris, A. 1992. On the correspondence between poroelasticity and thermoelasticity. *Journal of Applied Physics* **71**(3): 1138-1141.
- Notay, Y. 2010. An aggregation-based algebraic multigrid method. *Electronic Transactions on Numerical Analysis* **37**(6):123-146.
- Notay, Y. 2012. Aggregation-based algebraic multigrid for convection-diffusion equations. *SIAM Journal on Scientific Computing* **34**(4): A2288-A2316.
- Ostensen, R. W. 1986. The effect of stress-dependent permeability on gas production and well testing. *SPE Formation Evaluation* **1**(3): 227-235. SPE-11220-PA. <http://dx.doi.org/10.2118/11220-PA>.
- Pruess, K. and Narasimhan, T.N. 1985. A practical method for modeling fluid and heat flow in fractured porous media. *SPE Journal* **25**(1): 14-26. SPE-10509-PA. <http://dx.doi.org/10.2118/10509-PA>.
- Pruess, K., Oldenburg, C. M., and Moridis, G. J. 1999. TOUGH2 User's Guide Version 2, <http://esd.lbl.gov/research/projects/tough/documentation/manuals.html> (accessed 3 April 2014)
- Renshaw, C. E. 1995. On the relationship between mechanical and hydraulic apertures in rough-walled fractures. *Journal of Geophysical Research: Solid Earth (1978–2012)* **100**(B12): 24629-24636.
- Rutqvist, J. 2011. Status of the TOUGH-FLAC simulator and recent applications related to coupled fluid flow and crustal deformations. *Computers & Geosciences* **37**(6): 739-750.

- Rutqvist, J., and Stephansson, O. 2003. The role of hydromechanical coupling in fractured rock engineering. *Hydrogeology Journal* **11**(1): 7-40.
- Rutqvist, J., and Tsang, C. F. 2003. TOUGH-FLAC: a numerical simulator for analysis of coupled thermal-hydrologic-mechanical processes in fractured and porous geological media under multi-phase flow conditions. *Proc.*, TOUGH Symposium, Berkeley, CA, 12-14 May, 12-14.
- Rutqvist, J., Wu, Y. S., Tsang, C. F., and Bodvarsson, G. 2002. A modeling approach for analysis of coupled multiphase fluid flow, heat transfer, and deformation in fractured porous rock. *International Journal of Rock Mechanics and Mining Sciences* **39**(4): 429-442.
- Settari, A. and Mourits, F. M. 1998. A coupled reservoir and geomechanical simulation system. *SPE Journal* **3**(3): 219-226. SPE-50939-PA. <http://dx.doi.org/10.2118/50939-PA>.
- Settari, A. and Walters, D. A. 2001. Advances in coupled geomechanical and reservoir modeling with applications to reservoir compaction. *SPE Journal* **6**(3): 334-342. SPE-74142-PA. <http://dx.doi.org/10.2118/74142-PA>.
- Tareke, F. 2002. Evaluation of wellbore parameters for well he-4, hellisheidi, sw-iceland. Geothermal Training in Iceland: Reports of the United Nations University Geothermal Training Programme in Iceland.
- Tester, J., et al. 2006. The Future of Geothermal Energy: Impact of Enhanced Geothermal Systems (EGS) on the United States in the 21st Century. Cambridge, MA: Massachusetts Institute of Technology.
- Tuminaro, R. S., Heroux, M., Hutchinson, S. A., and Shadid, J. N. 1999. Official Aztec User's Guide, <http://trilinos.org/oldsite/packages/aztecoo/AztecOOUserGuide.pdf> (accessed 14 June 2014).
- Wallis, J. R. 1983. Incomplete Gaussian elimination as a preconditioning for generalized conjugate gradient acceleration. Presented at the SPE Reservoir Simulation Symposium, San Francisco, California, 15-18 November. Society of Petroleum Engineers. SPE-12265-MS. <http://dx.doi.org/10.2118/12265-MS>.
- Wallis, J. R., Kendall, R. P., and Little, T. E. 1985. Constrained residual acceleration of conjugate residual methods. Presented at the SPE Reservoir Simulation Symposium, Dallas, Texas, 10-13 February. SPE-13536-MS. <http://dx.doi.org/10.2118/13536-MS>
- Walsh, J. B. 1981. Effect of pore pressure and confining pressure on fracture permeability. *International Journal of Rock Mechanics and Mining Sciences and Geomechanics Abstracts* **18**(5):429-435. Pergamon.

- Wang, S., Xiong, Y., Winterfeld, P., Zhang, K., and Wu, Y. S. 2014. Parallel Simulation of Thermal-Hydrological-Mechanic (THM) Processes in Geothermal Reservoirs. Presented at the 39th Geothermal Workshop, Stanford, CA, 24-26 February.
- Warren, J. E. and Root, P. J. 1963. The Behavior of Naturally Fractured Reservoirs. *SPE Journal* **3**(03): 245-255. SPE-426-PA. <http://dx.doi.org/10.2118/426-PA>.
- Wilson, R. K., and Aifantis, E. C. 1982. On the theory of consolidation with double porosity. *International Journal of Engineering Science* **20**(9): 1009-1035.
- Winterfeld, P. H., and Y. S. Wu. 2011. Parallel simulation of CO₂ sequestration with rock deformation in saline aquifers. Presented at the SPE Reservoir Simulation Symposium, Woodlands, Texas, 21-23 February. SPE-141514-MS. <http://dx.doi.org/10.2118/141514-MS>.
- Winterfeld, P. H. and Wu, Y. S. 2014. Simulation of CO₂ Sequestration in Brine Aquifers with Geomechanical Coupling. In *Computational Models for CO₂ Sequestration and Compressed Air Energy Storage*, ed. J. Bundschuh and R. Al-Khoury, Chap. 8. Boca Raton, Florida: CRC Press.
- Winterfeld, P. H., Wu, Y. S., Zhang, R., Fakcharoenphol, P., and Xiong, Y. 2013. Coupled geomechanical and reactive geochemical model for fluid and heat flow: application for enhanced geothermal reservoir. Presented at the SPE Reservoir Characterization and Simulation Conference and Exhibition, Abu Dhabi, UAE, 16-18 September. SPE-165982-MS. <http://dx.doi.org/10.2118/165982-MS>.
- Witherspoon, P. A., Amick, C. H., Gale, J. E., and Iwai, K. 1979. Observations of a potential size effect in experimental determination of the hydraulic properties of fractures. *Water Resources Research* **15**(5): 1142-1146.
- Witherspoon, P. A., Wang, J. S. Y., Iwai, K., and Gale, J. E. 1980. Validity of cubic law for fluid flow in a deformable rock fracture. *Water Resources Research* **16**(6): 1016-1024.
- Wu, Y. S. 1998. MSFLOW: multiphase subsurface flow model of oil, gas and water in porous and fractured media with water shut-off capability, Documentation and User's Guide. Twange Int., Houston, Tex., Walnut Creek, Calif.
- Wu, Y. S., and Pruess, K. 1988. A multiple-porosity method for simulation of naturally fractured petroleum reservoirs. *SPE Reservoir Engineering* **3**(1): SPE-15129-PA. <http://dx.doi.org/10.2118/15129-PA>.
- Wu, Y. S., Zhang, K., Ding, C., Pruess, K., Elmroth, E., and Bodvarsson, G. S. 2002. An efficient parallel-computing method for modeling nonisothermal multiphase flow and multicomponent transport in porous and fractured media. *Advances in Water Resources* **25**(3): 243-261.

Wu, Y. S., Di, Y., Kang, Z., and Fakcharoenphol, P. 2011. A multiple-continuum model for simulating single-phase and multiphase flow in naturally fractured vuggy reservoirs. *Journal of Petroleum Science and Engineering* **78**(1): 13-22.

Zhang, K., Wu, Y. S., and Pruess, K. 2008. User's guide for TOUGH2-MP: a massively parallel version of the TOUGH2 code. Report LBNL-315E, Lawrence Berkeley National Laboratory, Berkeley, CA.

APPENDIX A

WATER PROPERTIES IN THM-EGS

In this chapter, the water properties, including viscosity, enthalpy and density, are plotted with respect to primary variables. Figure A-1 shows the viscosity profile. We can see that as temperature increase, water viscosity decrease. Figure A-2 shows the enthalpy profile. As the figure indicates, water enthalpy increases when the system temperature and/or pressure increases. Figure A-3 shows the water density profile. From the figure we can see that water density is not sensitive to temperature and pressure change.

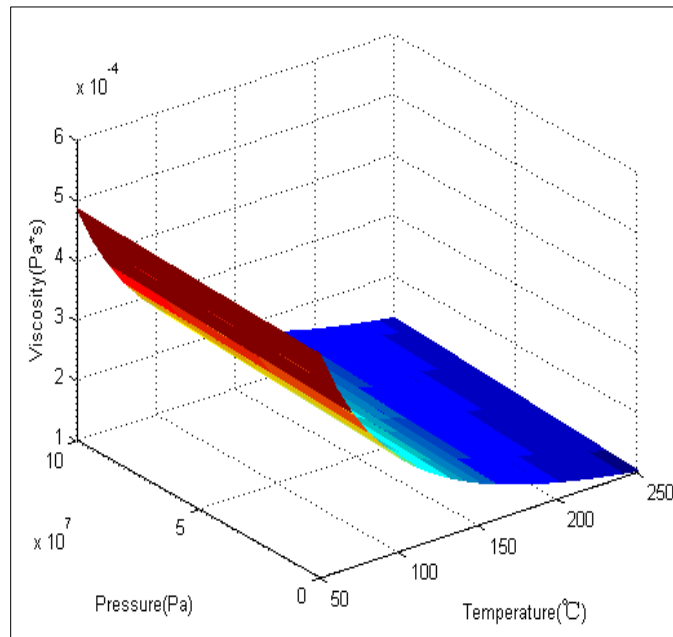


Figure A-1 Viscosity of water phase.

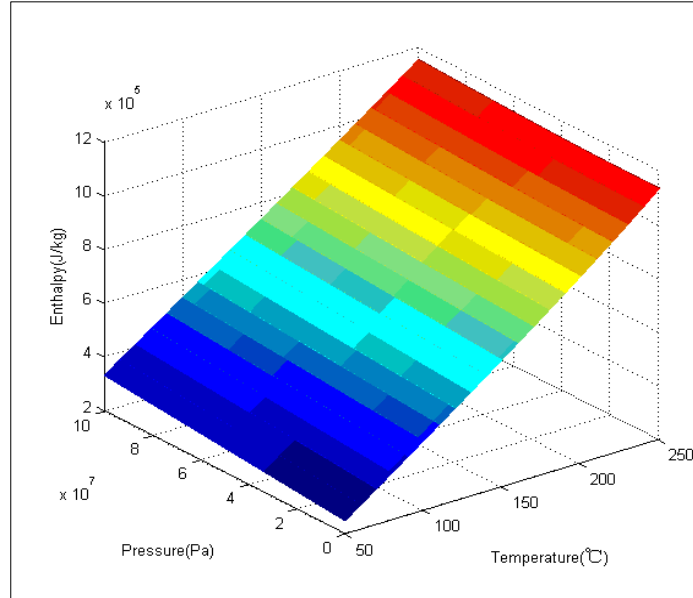


Figure A-2 Enthalpy of water phase.

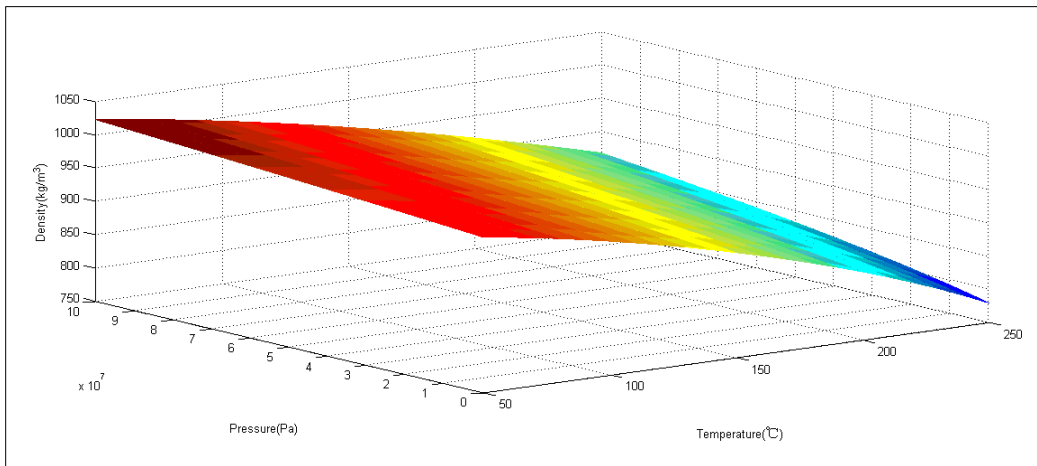


Figure A-3 Density of water phase.

APPENDIX B

GAS PROPERTY IN THM-EGS

In this chapter, the gas phase properties, including internal energy and viscosity, are plotted with respect to primary variables. Figure B-1 shows the internal energy profile of the air-vapor system, from which we can see that the internal energy of gas phase is sensitive to both pressure and temperature. Figure B-2 shows the viscosity of the air-vapor system. In the surface on the top, the mass fraction of air component is 60%, while in the surface on the bottom, the mass fraction of air component is 1%. It means that at given temperature and pressure condition, the less air component in the gas phase, the less viscous the gas phase is.

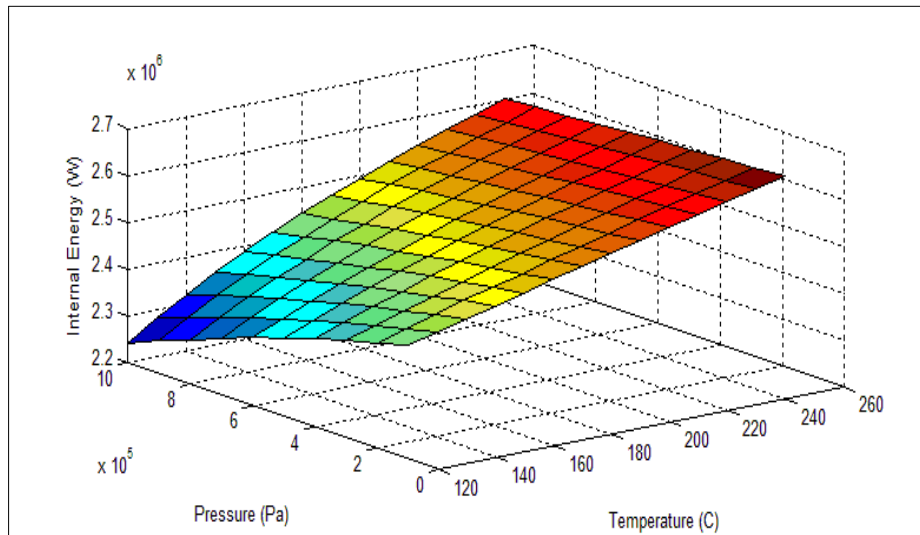


Figure B-1 Internal energy of air-vapor mixture.

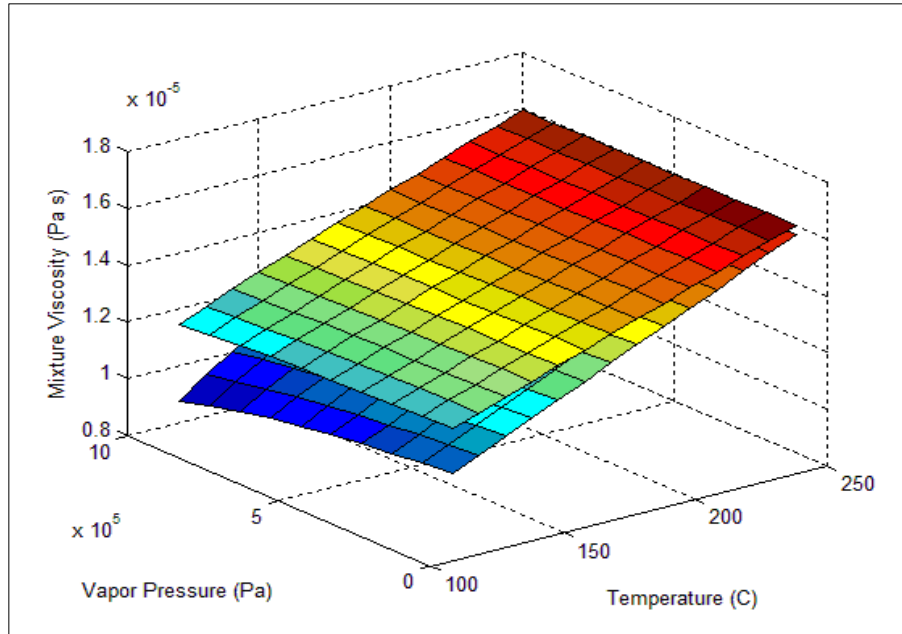


Figure B-2 Viscosity of air-vapor mixture. Top: mass fraction of air=0.6; bottom: mass fraction of air =0.01.

APPENDIX C

AN EXAMPLE INPUT FILE FOR THM-EGS

In this chapter, an example of the input file of THM-EGS is provided, as shown in Figure

C-1.

```

1  +HYDRAULIC WELL PAIRS
2  ROCKS-----1-----2-----3-----4-----5-----6-----7-----8
3  XXXX 5      2700.      .01      1.e-13      1.e-13      1.e-13      5.51      1000.
4      3.e-10      3.e-4      0.
5      3          0.20      0.01
6      7          0.20      .25      .00084      1.e5      1.
7      4  4      0          0.25      4.5e10      1.0
8      0  0      80.      500.      70.      3.000E07      3.000E07      3.000E07      0.64
9  XXXX 5      2600.      .02      1.e-13      1.e-13      1.e-13      2.51      1000.
10     1.e-10      1.e-3      0.
11     3          0.20      0.01
12     7          0.20      .25      .00084      1.e5      1.
13     4  4      0          0.25      4.5e12      1.0
14     0  0      80.      500.      70.      8.000E07      8.000E07      8.000E07      1.64
15
16  ICOUP-----1-----2-----3-----4-----5-----6-----7-----8
17  ..... 1          0
18
19  START-----1-----2-----3-----4-----5-----6-----7-----8
20  -----1 MOP: 123456789+123456789+1234 -----5-----6-----7-----8
21  PARAM-----1-----2-----3-----4-----5-----6-----7-----8
22  39999      10010 030100020000400 23
23  ..... 2.15E07      100.      2.e5
24  ..... 1.e-8
25  ..... 7.000e7          0.00          90.
26  TIMES-----1-----2-----3-----4-----5-----6-----7-----8
27
28
29  FOFT  ---1-----2-----3-----4-----5-----6-----7-----8
30  000ST
31  000A9
32
33  GRMOD-----1-----2-----3-----4-----5-----6-----7-----8
34  COEFS          45      1      1      1      1
35  STRES          1      27      1      1      1      45      1.000e8
36  COEFS          45      1      1      1      1
37  STRES          1      27      1      1      1      45      1.000e8
38
39  GENER
40  0009TINJ 1          1      MASS      2.00      0.20E+06      0.000      0
41  000A9PRO 1          1      DELV      5.0E-14      0.50E8
42
43  INCON-----1-----2-----3-----4-----5-----6-----7-----8
44  -----1960 through 2004+-----8
45  GOFT
46  000ST
47
48  ENDCY-----1-----2-----3-----4-----5-----6-----7-----8
49
50

```

Figure C-1 An example input file of THM-EGS.